Synoptic processes of winter precipitation in the Upper Indus Basin

Jean-Philippe Baudouin[1,2], Michael Herzog[2], and Cameron A. Petrie[3]

[1]Department of Environmental Physics, Heidelberg University, Germany
[2]Department of Geography, University of Cambridge, United Kingdom
[3]Department of Archaeology, University of Cambridge, United Kingdom

Correspondence: Jean-Philippe Baudouin (baudouin.jeanphilippe@gmail.com)

Abstract.

Precipitation in the Upper Indus Basin is triggered by orographic interaction and the forced uplift of a cross-barrier moisture flow. Winter precipitation events are particularly active in this region and are driven by an approaching upper troposphere Western Disturbance. Here statistical tools are used to decompose the winter precipitation timeseries into a wind and a moisture contribution. The relationship between each contribution and the Western Disturbances are investigated. We find that the wind contribution is not only related to the intensity of the upper troposphere disturbances but also to their thermal structure through baroclinic processes. Particularly, a short-lived baroclinic interaction between the Western Disturbance and the lower altitude cross-barrier flow occurs due to the shape of the relief. This interaction explains both the high activity of Western Disturbances in the area, as well as their quick decay as they move further east. We also revealed the existence of a moisture pathway from the Red Sea, to the Persian Gulf and the north of the Arabian Sea. A Western Disturbance strengthens this flow and steers it towards the Upper Indus Plain, particularly if it originates from a more southern latitude. In cases where the disturbance originates from the north-west, its impact on the moisture flow is limited, since the advected continental dry air drastically limits the precipitation output. The study offers a conceptual framework to study the synoptic activity of Western Disturbances as well as key parameters that explain their precipitation output. This can be used to investigate meso-scale processes or intra-seasonal to inter-annual synoptic activity.

1 Introduction

The Upper Indus River Basin (UIB, Figure 1) is a mountainous region that differs from the rest of the Indian subcontinent for the large amount of precipitation it receives outside of the summer monsoon season (56% or 505mm between October and May for ERA5 on the period 1979 and 2018, Baudouin et al., 2020b). Much of this precipitation falls as snow at altitude during the coldest part of the season (Hewitt, 2011; Dahri et al., 2018; Baudouin et al., 2020b). The precipitation and the snowmelt later in the season are key for mitigating the seasonal drought that occurs for most of South Asia before the arrival of the summer monsoon (Singh et al., 2011; Dimri et al., 2015; Rana et al., 2015).

In either winter or summer, most of the precipitation in the UIB is triggered by orographic interaction, and more specifically, by the forced up-lift of a moisture transport perpendicular to the mountain ranges (Baudouin et al., 2020a). However, the synoptic drivers of cross-barrier transport differ between summer and winter. The winter drivers have been discussed since the

mid-twentieth century (Malurkar, 1947; Mull and Desai, 1947, cf. in Dimri et al. 2015). Winter precipitation events in the UIB are in general related to the passing of extra-tropical, synoptic-scale, disturbances often originating from the Mediterranean Sea, the Black Sea, or the Caspian Sea, and referred to as Western Disturbances (WDs, Dimri et al., 2015; Hunt et al., 2018a). Many numerical case studies have investigated the characteristics of WD's and their interaction with the relief (e.g. Dimri, 2004;

30   Dimri and Niyogi, 2013; Thomas et al., 2018; Krishnan et al., 2018). More recently, exhaustive tracking analysis have been carried out on generalised previous results (Syed et al., 2010; Cannon et al., 2016; Hunt et al., 2018a). Despite the abundant interest, the general physical processes explaining the relationship between WD characteristics and precipitation variability are not well enough understood.

Typically up to six or seven WDs occur per month (Hunt et al., 2018a), although lower frequencies have been observed

35   (Cannon et al., 2015; Dimri, 2013), probably depending on threshold intensity. A WD is characterised by a maximum of vorticity or a minimum in geopotential height near the tropopause between $325\,\mathrm{hPa}$ (Hunt et al., 2018a) and $200\,\mathrm{hPa}$ (Midhuna et al., 2020). The cyclonic circulation around the WDs interacts with the relief to trigger precipitation (Baudouin et al., 2020a). Generally, a stronger cyclonic circulation induces more precipitation (Hunt et al., 2018a). Yet, the convergence triggering precipitation occurs at a much lower altitude, around $700\,\mathrm{hPa}$ and below (Hunt et al., 2018a; Baudouin et al., 2020a), which

40   suggests that the downward propagation of the cyclonic circulation is key to producing precipitation. Alternatively, Dimri and Chevuturi (2014) have proposed that the WDs interact with a pre-existing low-level cyclonic circulation located over the Thar desert, reminiscent of the heat low present in the area during summer (Bollasina and Nigam, 2011). The baroclinic interaction between an upper- and a lower-level trough is known to be a key process in the growth of extra-tropical disturbances (Malardel, 2005). Furthermore, Hunt et al. (2021) show that interactions between WDs and tropical depression exist, although these are

45   not common in winter.

The upper troposphere disturbance characterising a WD is embedded in the Subtropical Westerly Jet (SWJ, Dimri et al., 2015; Hunt et al., 2018a). The SWJ characterises the Northern edge of the Hadley circulation (Krishnamurti, 1961). In Asia, the Tibetan Plateau disrupts the SWJ. The jet oscillates between two stable states: one north of the Tibetan Plateau, always present in summer, and one south of it, reached only in winter (Schiemann et al., 2009). Furthermore, in winter, the SWJ is also

50   split in two climatological jet streaks of higher intensity (Krishnamurti, 1961; Schiemann et al., 2009): one over the Arabian Peninsula (Arabian Jet, Yang et al., 2004; de Vries et al., 2016), and the other over East Asia (East Asian Jet, Xueyuan and Yaocun, 2005). It has been argued that the position and strength of the SWJ influences WD intensity at the intra-seasonal and inter-annual scale (Filippi et al., 2014; Dimri et al., 2015; Hunt et al., 2018a; Ahmed et al., 2019). These studies suggest that the higher kinetic energy in the SWJ is able to fuel the development of WDs as for other baroclinic waves. Yet, Hunt et al.

55   (2018a) have mentioned that WDs are immature baroclinic waves that differ from their mature counterpart in the Atlantic or Pacific Ocean: the WDs remain in a nascent state without low-level warm core or frontal activities. The coupling between the SWJ, WDs and the relief needs to be better characterised as they greatly influence vertical velocities, in part through baroclinic processes, and thus precipitation. In particular, this coupling could explain why WDs are particularly active in the UIB.

While wind is the most important parameter to explain precipitation synoptic variability, moisture content modulates the

60   strength of the relationship (Baudouin et al., 2020a). Previous studies have investigated moisture transport in the context of

winter precipitation in the UIB using moisture flux (Dimri, 2007; Syed et al., 2010; Filippi et al., 2014; Hunt et al., 2018a) or back trajectories (Jeelani et al., 2018; Hunt et al., 2018b; Boschi and Lucarini, 2019). Yet, some uncertainty remains about the moisture sources for precipitation and its pathways. The Arabian Sea is often suggested as the primary source of moisture (Dimri, 2007; Filippi et al., 2014; Hunt et al., 2018b). Less certain is the input of moisture from the Mediterranean Sea, as it

65 is sometimes suggested that it is the origin of the most intense WDs that reach the UIB (e.g. Filippi et al., 2014; Dimri et al., 2015). Occasionally, the Red Sea (Dimri, 2007; Filippi et al., 2014), the Caspian Sea (Syed et al., 2010; Dimri and Niyogi, 2013) or even the Atlantic Ocean (Dimri et al., 2015) are also mentioned. The moisture pathway is certainly affected by the passing of a WD, through the deformation of the low-level wind field the WD imposes (Baudouin et al., 2020a). Yet, the reason for moisture variability at the synoptic scale has not been investigated extensively.

70 The objective of this study is to understand the synoptic variability of winter precipitation in the UIB and how this relates to various characteristics of WDs. The analysis makes use of reanalysis data and extends statistical tools developed in Baudouin et al. (2020a, section 3). The analysis particularly focuses on understanding the origin of cross-barrier wind variability and moisture sources.

2 Season, data and study area

75 The timeseries of precipitation considered here is defined by a 3-hourly average over the UIB (see dashed contour in Figure 1). This study area is the same as the one used in Baudouin et al. (2020a) and Baudouin et al. (2020b). Both precipitation and atmospheric variables are derived from ERA5 reanalysis, at a 3-hourly intervals and 0.5° resolution, over the 40-year period 1979-2018. ERA5 proved to provide a good representation of precipitation variability (Baudouin et al., 2020b) and synoptic processes (Baudouin et al., 2020a). ERA5 data provide extrapolated values on pressure levels below the model surface which

80 will be excluded from the analysis. Consequently, grid points where their all-time minimum geopotential is above the model surface were deselected[1].

All analyses are performed over an extended winter season that spans from October to May. Similar studies on WDs generally considered a shorter winter period to avoid the dry intermediate seasons (e.g. December-February in Midhuna et al. 2020 or December-April in Hunt et al. 2018b). However, it is possible to demonstrate that large precipitation events during these

85 intermediate seasons are driven by the same synoptic disturbances as in winter (cf. Baudouin, 2020, Figure 4.18). This selection also increases the diversity of background conditions that are considered.

---

[1]This is in contrast to Baudouin et al. (2020a), which used an arbitrary pressure threshold
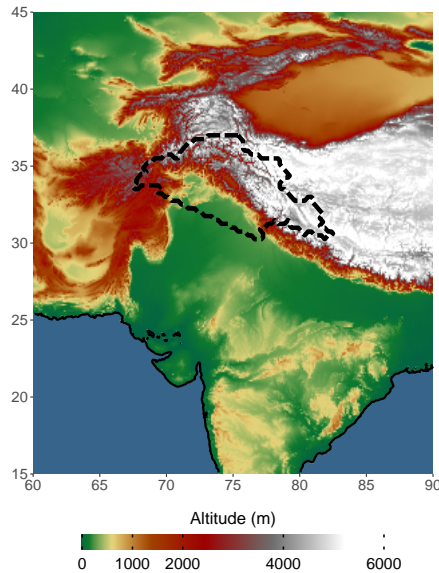
Figure 1. Map of the relief of South Asia. The study area (Upper Indus Basin, UIB) is indicated by the dashed line.

3 Methods

3.1 Computing wind and moisture contributions to precipitation

Baudouin et al. (2020a) demonstrated the ability of principal component (PC) regression to analyse the precipitation variability
in terms of moisture transport, defined as the product of wind (both components) and specific humidity. A similar method is
used here, with small differences, to both simplify and test the robustness of the method. The reasons for each of the changes
in the approach and their impact on the coefficient of determination (or explained variance) of the regression is further detailed
in Baudouin (2020).

The method uses moisture transport at $700\,\mathrm{hPa}$ to predict 3-hourly precipitation between October and May. Moisture trans-
port is considered over an area between 18 and $36°$N and between 67 and $85°$E, for a resolution of $0.5°$ (see the extent and
resolution in Figure 2-A). The PC analysis is applied on centred timeseries of moisture transport and considers both meridional
and zonal components simultaneously. The first 46 PCs are selected for the regression. [2] z The prediction of precipitation is
a linear combination of the PCs of moisture transport. However, since precipitation can only be positive, negative predictions
are fixed to 0. This condition is directly applied to the statistical model of the regression, which is solved using an iterative
optimisation method (Brent, 1973). Finally, a condition to correct any bias is also added to the statistical model. The coefficient
of regression of this regression is $R^2 = 0.878$ which is very close to the one found in Baudouin et al. (2020a, $R^2 = 0.832$).

---

[2]hlThis number insures the "extent of pattern" as defined in Baudouin et al. (2020a), see also Baudouin (2020)
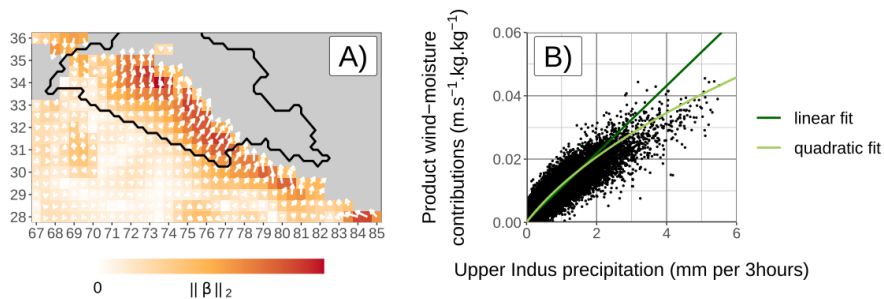
Figure 2. Results of the wintertime regression of precipitation with meridional and zonal moisture transport at $700\,\text{hPa}$. Precipitation is defined as the 3-hourly averaged over the UIB (black contour Panel A). Panel A shows the coefficients associated with each predictor. The arrows indicate the most efficient direction of moisture transport, while the length and the colour of the arrows indicate the total weight of moisture transport (i.e. the Euclidean norm of the coefficients from both zonal and meridional components). The exact values of the coefficients are not interpretable and are therefore not indicated. Panel B is the scatter plot of the product of wind and moisture contributions against precipitation, with the green lines representing two types of fit.

Figure 2-A shows the coefficients of the regression: the arrows are constructed from the coefficients of each component, while the colour is proportional to the length of the arrow. The arrows highlight the moisture convergence zone along the Himalayan foothills that triggers precipitation (cf. Baudouin et al., 2020a).

105   As in Baudouin et al. (2020a), the prediction is split between the contribution of wind and moisture, using a weighted spatial averaging. The wind contribution (labelled hereafter $UV700$) is computed by multiplying the time series of meridional and zonal wind with the respective meridional and zonal regression coefficients and summing the result. $UV700$ is interpreted as the cross-barrier wind effect on the precipitation. For the moisture contribution (labelled hereafter $Q700$), the time series of specific humidity at each location are weighted with the Euclidean norm of the coefficients of both meridional and zonal

110   moisture transport (i.e. the colour scheme used in Figure 2-A). After fixing negative values of $UV700$ to 0, the product of $Q700$ and $UV700$ has an R^2 of 0.844 with precipitation, close to the R^2 of the regression with moisture transport (0.878), despite the spatial averaging. Note that the intercept of the regression with moisture transport equals $0.14\,\text{mm}\cdot 3\text{hours}^{-1}$, but is not taken into account when considering the product of $Q700$ and $UV700$.

     Figure 2-B shows the product of $Q700$ and $UV700$, against precipitation. A non-linearity can be seen as precipitation

115   increases quicker than the product. This non-linearity is not present when including moisture transport at $850\,\text{hPa}$ in the PC regression (cf. Baudouin et al., 2020a). This behaviour can be explained by the fact that moisture transport at lower altitude is not proportional to that of higher altitude and instead quickly increases once strong moisture transport is already present at $700\,\text{hPa}$ (Baudouin et al., 2020a). An ad hoc quadratic fit of the precipitation with the product of $Q700$ and $UV700$ captures the non-linearity and slightly increases the R^2 from 0.844 to 0.853. Hence, the product of $Q700$ and $UV700$ is a good predictor

120   of precipitation and each contribution will be investigated separately in the following sections.

3.2 Relating cross-barrier wind to Western Disturbances

The second methodological step consists in using $UV700$ to investigate the link between the cross-barrier wind intensity and various WDs characteristics.

First, a qualitative analysis is proposed using a composite. The composite is defined as the average over atmospheric fields of the time steps with the 10% highest value of $UV700$ (i.e. 3-hourly $UV700$ above $2.68\,\mathrm{m\,s^{-1}}$). This selection of time steps accounts for about 50% of the precipitation between October and May. To remove the influence of the seasonality, the anomalies of the atmospheric fields are computed by removing the four first harmonics of the seasonal cycle. This approach ensures, for example, that the monthly mean anomalies of geopotential height at $300\,\mathrm{hPa}$ are below $10\,\mathrm{gpm}$. Various pressure-level fields are investigated: the geopotential height anomaly at $300\,\mathrm{hPa}$ and the anomaly of geopotential thickness between $500\,\mathrm{hPa}$ and $300\,\mathrm{hPa}$ (Figure 3); the wind speed and wind speed anomaly at $250\,\mathrm{hPa}$ (Figure 5); the precipitable water anomaly and the absolute water vapour flux (Figure 10-B to G); the evaporation anomaly and absolute 10m sea wind (Figure 11-B to D). For a vertical cross-section of the troposphere along $30°$N (see white horizontal line in Figure 3-A) we also investigate the anomaly of geopotential height, temperature, specific humidity and meridional wind (Figure 4). The section cuts across the Indus Plain between $70°$and $78°$E, just south of the UIB, where the southerly advection originates. In each figure, the lead/lag is relative to the timesteps selected for the composite.

For a more quantitative approach, a PC regression is used, similar to the one developed in the previous section, but with different variables. The regression predicts $UV700$ using 3-hourly time series of three different 2D fields: geopotential height at $300\,\mathrm{hPa}$, geopotential height thickness between 700 and $500\,\mathrm{hPa}$, and between 500 and $300\,\mathrm{hPa}$. The predictors are taken within a box between $50°$ and $90°$E, and between $20°$ and $50°$N at $1°$resolution [3] except for the lowest thickness where grid points whose maximal surface pressure is above $700\,\mathrm{hPa}$ are removed (see the extent of the colour shading shown in Figure 6-B, C, and D). Both positive and negative values of $UV700$ are predicted. The time series of the predictors are standardised (i.e. the mean is removed and the result divided by the standard deviation), and the PC decomposition is then performed independently for each 2D field. Finally, the regression makes use of the first 40 PCs of each 2D fields, for a total of 120 predictors.

The regression has a high predictive skill, with $R^2 = 0.886$. The scatter plot of $UV700$ against its prediction shown in Figure 6-A also suggests that the prediction is successful for a wide range of values of $UV700$, despite some underestimations for the highest values. The coefficients of the regression are displayed in Figure 6-B, C and D. The partial prediction of $UV700$ associated with each of the three fields are called $Z300$ for the geopotential at $300\,\mathrm{hPa}$, and dZ_UP and dZ_LW for the geopotential thickness between the layers 500-300 hPa and 700-500 hPa respectively. Note that a more detailed explanation of the methodology is available in Baudouin et al. (2020a) and Baudouin (2020).

The geopotential height at $300\,\mathrm{hPa}$ has been used for tracking analysis (Cannon et al., 2016) and WD indices (Madhura et al., 2015; Midhuna et al., 2020) to characterise WDs. However, only using geopotential heights as predictors limits the predictive skill ($R^2 = 0.678$), and leads to an underestimation of $UV700$ for values above $2.5\,\mathrm{m\,s^{-1}}$ (Baudouin, 2020). This

---

[3]Higher resolution is not needed and requires significantly higher computational power.

issue is corrected by adding geopotential height thicknesses as predictors. That way, the regression can be interpreted as the decomposition of the wind at 700 hPa into the wind at 300 hPa and the windshear between the two layers.

155   We noticed that dZ_UP and dZ_LW are negatively correlated with the predictant $UV700$. In regression studies, predictors exhibiting such a behaviour are referred to as a suppressor: the predictor suppresses the variability of one or several other predictors (Smith et al., 1992; Nathans et al., 2012). In this case, dZ_UP and dZ_LW suppress some of the variability of $Z300$. To simplify the analysis, a new contribution of the geopotential thickness to the wind is computed. dZa_UP is the residual of the regression of dZ_UP with $Z300$: the variability of $Z300$ is removed from dZ_UP. It describes the anomalous

160 geopotential thickness given the situation of the geopotential at 300 hPa. The same is performed for dZ_LW. The regression is summarised in the equation below, with $\widehat{UV700}$ as the prediction of $UV700$:

$$
\begin{aligned}
\widehat{UV700} &= \beta_0 + Z300 + dZ\_UP + dZ\_LW \\
&= \beta_0 + Z300 + (a \times Z300 + dZa\_UP) + (b \times Z300 + dZa\_LW) \\
&= \beta_0 + (1 + a + b) \times Z300 + dZa\_UP + dZa\_LW
\end{aligned}
\tag{1}
$$

    Note that $Z300$ is recomputed hereafter so that it includes the fractions a and b derived from dZ_UP and dZ_LW, respectively. Note also the presence of the constant offset β_0. The same composites based on the highest value of $UV700$ as above

165 are used to investigate the evolution of those contributions during a peak of $UV700$ (Figure 7).

3.3 Investigating variability in WD structure

There is variability in the dynamic structure of WDs. To investigate this variance, a more complex composite analysis is used, based on two quantile regressions. To maintain comparability with the other composite analysis (cf. Section 3.2), the regressions are performed using the timesteps whose value of $UV700$ is above the 90th percentile[4]. The quantile regressions predict

170 respectively the first and third quartile of $\widehat{UV700}$. $\widehat{UV700}$ (see Equation 1) is preferred to $UV700$ itself, so that the differences between the two subsets are not related to the variability missed by the PC regression of $UV700$ with geopotential heights and thicknesses. We regress the values of $\widehat{UV700}$ at the selected timesteps on several predictors: $Z300$, geopotential anomaly at 300hPa at the centre of the mean WD (66°E - 36°N), and months. Two subsets are eventually created that include all the timesteps whose value of $\widehat{UV700}$ is conditionally below the first and above the third quartile respectively. These two subsets

175 are used as composite and hereafter referred to as "Lower UV700" and "Higher UV700". The properties of the quantile regression ensure that the two composites have the same averaged characteristics regarding the predictors (or conditions), but a mean value of $\widehat{UV700}$ as different as possible. Hence, the inclusion of $Z300$ and geopotential anomaly as predictors guarantee that the composite WD in each subset is located at a similar place and has a similar intensity. Months are also included to avoid seasonal biases regarding WD characteristics: for each month, the same number of timesteps is present in each subset. Figures

180 8 and 9 represent the same variables as in Figures 3 and 5. respectively but are based on these new composites.

---

[4]This is the usual quantile and is not based on a quantile regression

Finally, a second sampling is performed to investigate the specific humidity variability in WDs. Two new subsets (hereafter and are computed based on two quantile regressions respectively predicting the first and third quartile of $Q700$. We regress the values of $Q700$ at the same timesteps as above. The predictors are the months, so as to remove the impact of seasonality, and the difference of the geopotential height anomaly between the grid points 60°E-36°N and 70°E-36°N. This latter predictor fixes the longitudinal gradient of geopotential across the UIB, and in this way, the position of the composite WD. However, the intensity of the WDs is not fixed as in the previous case. Various composites are derived from these selections: Figures 12, and 13, respectively comparable to Figures 10 and 3.

4 Results on the wind contribution

4.1 WD characteristics

4.1.1 The upper troposphere disturbance

High $UV700$ is associated with a negative geopotential anomaly (i.e. cyclonic disturbances) with the minimum located at 36°N 66°E, just north of the Hindu Kush, and north-west of the UIB (Figure 3-B), and near the tropopause, at around $300\,\text{hPa}$ (Figure 4-B), in agreement with previous studies (Hunt et al., 2018a; Midhuna et al., 2020). The lead/lag analysis (Figures 3-A, 3-C, 4-A, and 4-C) reveals an eastward motion of the disturbance. Both characteristics fit the definition of Western Disturbances (WDs).

Interestingly, there is no evidence of a separate cyclonic circulation near the surface, neither on the day of high $UV700$ (Figure 4-B), nor the day before (Figure 4-A), as mentioned by Dimri and Chevuturi (2014) and Dimri et al. (2015) among others. Instead, Figure 4-B shows that the lower altitude circulation is simply a weaker extension of the anomaly at $300\,\text{hPa}$. This downward extension of the cyclonic circulation is also evident in the meridional wind field (Figure 4-D). However, Dimri and Chevuturi (2014) might have referred to fast-moving small-scale eddies that can circulate near the surface of the Indus Plain and are not detected by the composite analysis.

4.1.2 The tropospheric cold core

The weakening of the cyclonic circulation towards the ground is due to a negative temperature anomaly: the WD has a cold core. The centre of the cold core is slightly displaced to the north-west of the geopotential anomaly minimum (Figure 3-B), which indicates baroclinicity. This baroclinicity is even clearer in Figures 4-A to C. There, a vertical black line indicates the location of the maximum anomaly for each altitude and broadly corresponds to the contour of zero meridional wind anomaly (Figure 4-D to F). The line exhibits a westward tilt with the altitude which is caused by the asymmetry between temperature and geopotential height, a characteristic of the baroclinic structure (Dimri and Chevuturi, 2014; Hunt et al., 2018a). The asymmetry further increases at lower altitude, below $700\,\text{hPa}$, where cold continental dry air is advected from Siberia and Central Asia at the rear of the WD (Figure 4, Yadav et al., 2012). The Sistan plain in eastern Iran forms a north-south valley between the Hindu Kush and the Iranian plateau, around 62°E in the cross-section, which funnels the cold air flow (Figure 4-B and
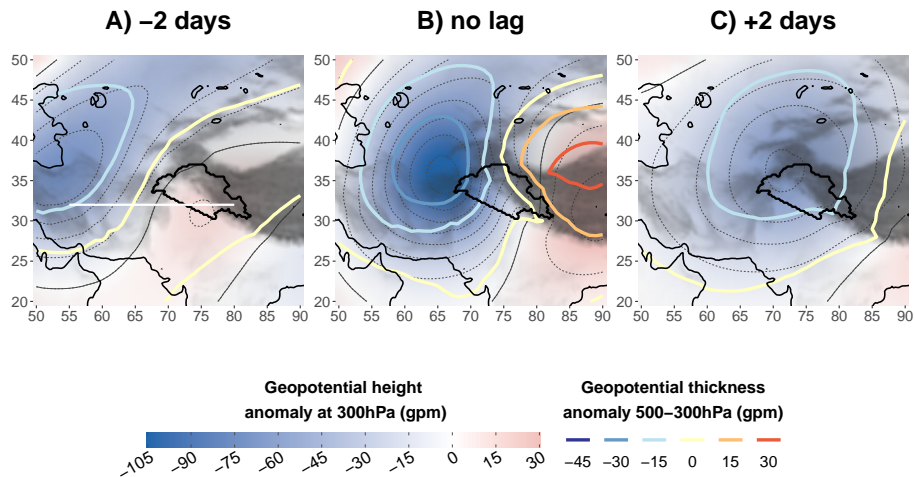
Figure 3. Composite maps of a geopotential height anomaly at 300 hPa (colour shading, thin contour lines every 15 gpm) and a geopotential thickness anomaly 500-300 hPa (thick contour lines). Values are an average based on the 10% highest values of the 700 hPa wind contribution during winter ($UV700$, panel B). For panel A (C) a two days lead (lag) is applied to the selection. The white line in panel A indicates the cross-section in Figure 4. Relief (grey shading) and coastline are based on ERA5 data. The UIB is indicated in each panel. Non-significant anomalies at the level 95% are shown in white (result of a t-test on the means). Note that the thickness anomaly is directly indicative of temperature anomalies in that layer under the hydrostatic equilibrium

E). Surprisingly, weaker but still negative temperature anomalies are also present in the Indus Plain, despite the southerly wind bringing in warmer air (Figure 4-B and E). This feature may be related to the adiabatic cooling (i.e. large scale upward motions) resulting from the baroclinic instability. Closer to the surface, precipitation evaporation and reduced solar radiation could further explain the cooling.

4.1.3 Linking the WDs to the upper-tropospheric wind: jet-stream and outflow

WDs are embedded in the Subtropical Westerly Jet (SWJ Dimri et al., 2015). The SWJ is present in winter at around 250 hPa and between 25°N and 35°N (see Figure 5 Schiemann et al., 2009). It exhibits two local maxima independent of WDs: the strongest south of Japan (East Asian Jet, above $55\,\mathrm{m\,s^{-1}}$), the other between Egypt and Iran (Arabian Jet, above $45\,\mathrm{m\,s^{-1}}$).

The mean WD centre is located just north of the jet, and drives a north-south dipole of wind speed anomaly that progresses eastward, following the WD motion (Figures 3 and 5). The positive wind anomaly results in the narrowing and strengthening of the Arabian Jet. Dimri et al. (2015) suggest that part of the strengthening could be due to the merging of the SWJ with the polar jet, which marks the limit between cold and warm air at the surface. This merging is not evident from the figure 5, but the composite analysis may hide this dynamic due to the highly variable position of the polar jet. After the peak of $UV700$, the
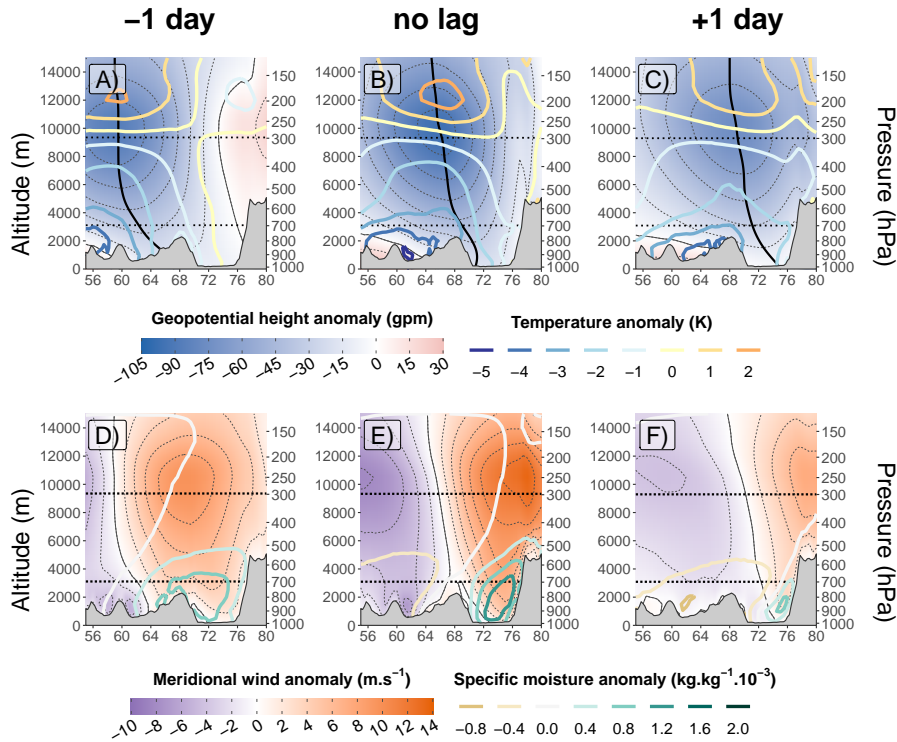
Figure 4. Composite cross-section along $30°$N of anomaly of geopotential height (colour shading, thin contour lines every 15 gpm) and temperature (thick contour line) in panels A to C, and meridional wind (colour shading, thin contour lines every 2 m s^{-1}) and specific moisture (thick contour line) in panels D to F. Values are an average based on the 10% highest values of $UV700$ (B, E). For panel A and D a one day lead is applied to the selection, while a one day lag is applied for panel C and F. The dotted horizontal lines represent the levels 700 and 300 hPa, the altitudes for the cross-barrier moisture transport in Figure 2 and minimum geopotential anomaly in Figure 3, respectively. The thick vertical black line in A, B, and C represents the longitude of the minimum geopotential anomaly as a function of altitude. The grey shading represents the relief as in ERA5. Note that the mean meridional wind is close to 0 except near the relief over the Tibetan and Iranian plateaus, where valleys funnel the mean westerly wind.

225 two parts of the dipole dissociate themselves: the negative northern anomaly slowly moves north-eastwards, while the positive anomaly quickly continues eastward, south of the Tibetan Plateau, carried by the SWJ (Figure 5-D).

When the lag is negative (Figure 5-A and B), the positive anomaly of wind speed further extends to the north-east, towards Central Asia, outside of the jet core. This deformation corresponds to the second stable position of the SWJ, north of the Tibetan Plateau, which is predominant in summer, but may also occurs in winter (jet split, Schiemann et al., 2009). A picture

230 from Pisharoty and Desai (1956), still in use in Dimri et al. (2015), suggests on the contrary that stronger wind speed occurs at altitude at the rear of a WD. While some WDs may have this characteristic, WDs triggering high $UV700$ and thus high precipitation do not exhibit that feature.
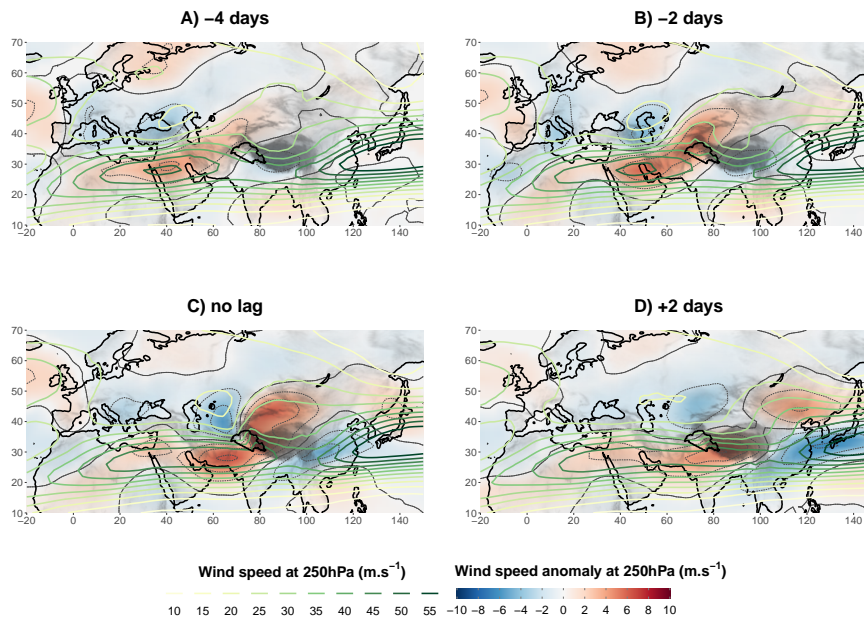
Figure 5. Composite maps of wind speed (thick contour lines) and wind speed anomaly (colour shading, thin contour lines every $2\,\mathrm{m\,s^{-1}}$) at $250\,\mathrm{hPa}$, based, for panel C on the same selection of the 10% highest $UV700$ as in Figure 3. For panel A, B and C, a 4 day lead, a 2 day lead, and a 2 day lag, is respectively applied to the fields. Non-significant anomalies at the level 95% are shown in white.

As the WD approaches the Tibetan Plateau, a second maximum positive anomaly of wind speed becomes evident over the high elevations: first over the Pamir range (Figure 5-B) and then along the Himalayas (Figure 5-C and D). This anomaly is in part the result of the increased funnelling of the jet over the high ground. At maximum $UV700$, this positive anomaly extends to the north-east of the WD and corresponds to the outflow of the cross-barrier wind in the UIB. The outflow is characterised by a swift anticyclonic turn, with strong similarity to the warm conveyor belt associated with mature baroclinic waves (Martínez-Alvarado et al., 2014). The increase in latitude and the latent heat release are both key to explaining that change in relative vorticity (Grams et al., 2011). The outflow can also be revealed by the analysis of the cloud cover and the development of large bank of cirrus (Agnihotri and Singh, 1982; Rakesh et al., 2009; Hunt et al., 2018a).

Finally, after the peak of $UV700$, the positive anomaly of wind speed related to the outflow completely splits from the circulation associated with the WD and continues eastward, north of the East Asian Jet. By contrast, the WD-relief interaction contributes to lower the intensity of the SWJ downwind: the East Asian Jet is notably weakened as a result (Figure 5-D). Meanwhile, the Arabian Jet remains anomalously strong; in fact, two days after the peak of $UV700$ the strength of the anomaly is about the same as four days before the peak. Hence, the increased intensity of the Arabian Jet is a longer-term feature that seems to promote the intensity or occurrence of a WD, but is not directly affected by the passing of one. This feature is evident from several intra-seasonal and inter-annual studies (Filippi et al., 2014; Hunt et al., 2018a; Ahmed et al., 2019). Hunt et al.

(2018a) also discussed the influence of the SWJ position on WDs, but the synoptic analysis presented here does not indicate that WDs are related to a change in the position of the Arabian jet.

4.2 Explaining $UV700$ variability using the PC regression

4.2.1 Interpretation of the PC regression

The results of the PC regression developed in Section 3.2 are presented using Figure 6. Two patterns are distinguishable in the coefficients for $Z300$ (Figure 6-B). The first is a dipole across the UIB, indicative of a geopotential gradient, which translates into a south-westerly geostrophic wind for positive $UV700$. The second, less clear, is a ring of positive coefficient around the negative centre of the dipole. The related gradient indicates a cyclonic anomaly for positive $UV700$, and therefore a WD. The extent of the ring can be interpreted as the effective radius of the centre of the anomaly in triggering a cross-barrier wind in the UIB. The centre of the pattern is located to the west of the study area, where the relief forms a notch important to trigger the vertical velocities (see Figure 1 in Baudouin et al., 2020a; see also Lang and Barros, 2004; Cannon et al., 2015). In conclusion, $Z300$ is representative of a cyclonic south-westerly geostrophic wind at $300\,\mathrm{hPa}$.

The coefficients associated with dZ_UP and dZ_LW are very similar and represent a dipole at a similar location as the one discussed for $Z300$ (Figure 6-C and D). The related gradient is equivalent to a north-easterly thermal wind, that is, an increase in south-westerly wind towards lower altitudes. However, the composite analyses showed that the cyclonic circulation associated with WDs weakens towards lower altitudes (Figure 4-B), and that the southerly wind is weaker closer to the surface (Figure 4-E). Indeed, dZ_UP and dZ_LW are negatively correlated with $Z300$. The new contributions dZa_UP and dZa_LW are designed so that they do not correlate with $Z300$ (cf. Section 3.2), rather they characterise the thermal structure of the WDs. If dZa_UP or dZa_LW are positive (negative) then the northwest-southeast temperature gradient over the UIB is weaker (stronger) than usual, and, consequently, the cold core of the WD is smoother, weaker, or further away (deeper or closer). These characteristics of the cold core are also evident from the composite maps for different $UV700$ intensity (Figure 8-B and E). The importance of the thermal structure has been little investigated previously. Midhuna et al. (2020) used geopotential thickness to characterise WD intensity. They suggested that a colder WD (a thinner 850-200 hPa layer) characterises a more intense WD. The analysis here, however, shows on the contrary that a WD with a warmer core than usual (or displaced cold core) produces stronger near surface dynamics that enhance precipitation.

Interestingly, the patterns for all predictors (Figure 6-B, C, and D) suggest that $UV700$ is sensitive to a geostrophic wind that is rotated by approximately $45°$ compared to the southerly wind that it is meant to predict (cf. Figure 2). Although the geopotential gradient is sufficient to predict wind intensity, it does not indicate the wind direction, which bends towards the lower pressures, as noted in Baudouin et al. (2020a). In this paper, it is suggested that this ageostrophic effect is caused by the drag along the Himalayan barrier and that it is key to trapping the cross-barrier flow in the notch formed at the intersection between the Himalayas and the Hindu Kush.

Finally, the regression successfully predicts the negative values of $UV700$ (Figure 6-A). These correspond to northerly divergent winds at $700\,\mathrm{hPa}$ in the UIB. The regression suggests that they are related to anticyclonic north-easterly geostrophic
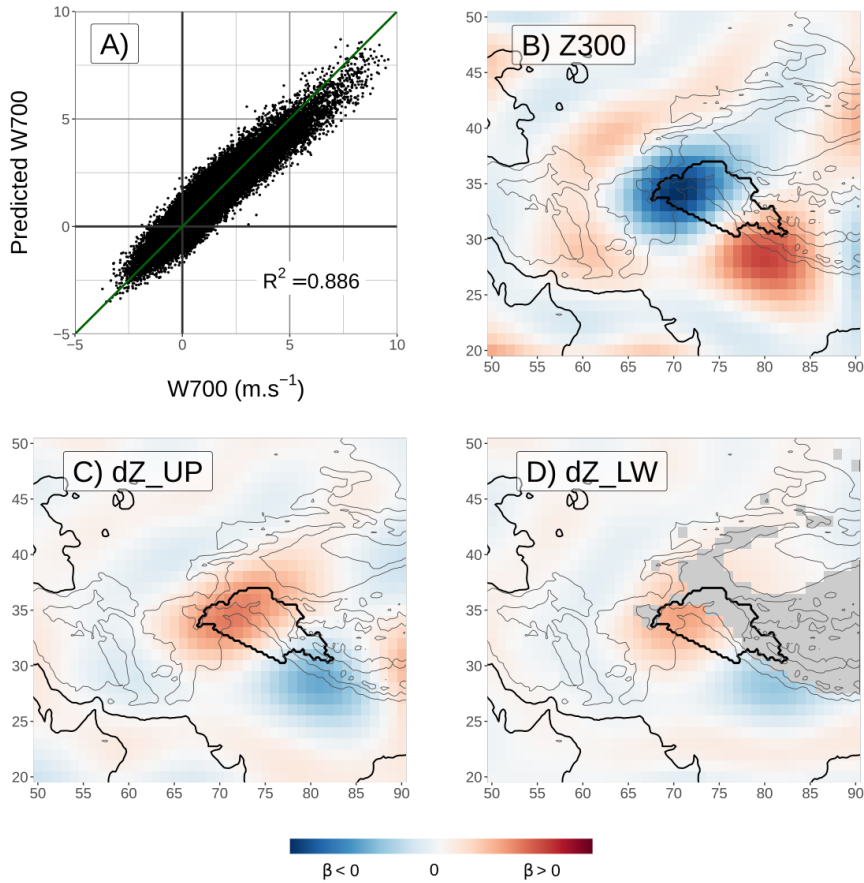
Figure 6. Results of the regression of 3-hourly $UV700$ with geopotential height at $300\,\mathrm{hPa}$ ($Z300$), geopotential thickness 500-300 hPa (dZ_UP), and geopotential thickness 700-500 hPa (dZ_LW). Panel A is the scatterplot between the predictand and the prediction. Panels B, C, and D show the coefficients associated with each predictor (cf. Baudouin et al., 2020a, equation 5). The exact values of the coefficients are not interpretable and are therefore not indicated.

winds. Since these winds are much less common than their south-westerly counterparts, large negative values of $UV700$ are rarer than positive ones. The regression also slightly underestimates the highest values of $UV700$, possibly because the larger latent heat release and increased buoyancy in the context of stronger convergence further sustains cross-barrier winds before the pressure gradient can adjust to it.

285 **4.2.2 Evolution of the partial predictions**

The different partial predictions of $UV700$ vary during a wind peak event as is evident in Figure 7. The peak value of $UV700$ (i.e. at no lag) is first due to dZa_UP (accounting for 46% of the predicted value), highlighting the importance of considering the WD thermal structure. $Z300$ is close behind (43%), while dZa_LW has a minor role (11%). Interestingly, $UV700$ (the
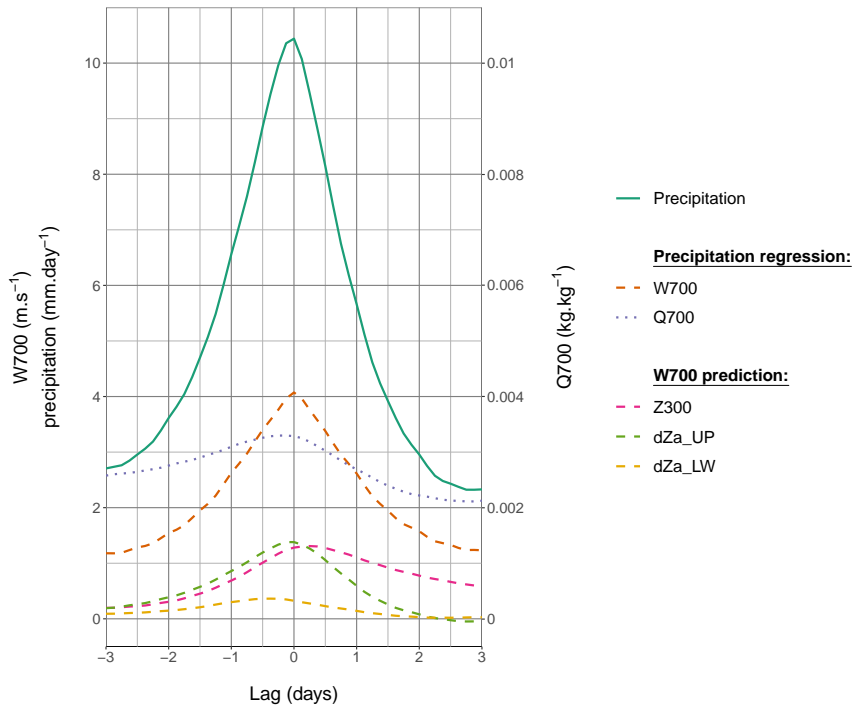
Figure 7. Lead/lag composite around the 10% highest values of $UV700$, as in Figures 3 4 and 5, for ERA5 precipitation, contributions to precipitation based on moisture transport ($UV700$, $Q700$, see Section 3.1), and partial prediction of $UV700$ based on geopotential ($Z300$) and geopotential thicknesses anomaly (dZa_UP and dZa_LW, see Section 3.2). Note that $Z300$, dZa_UP, and dZa_LW have the same units as $UV700$, and, with the intercept, add up to the prediction of $UV700$ ($\widehat{UV700}$, see Equation 1).

dashed orange line) rises and decays symmetrically around its peak. However, this is not the case for its different partial predictions (other dashed lines). All partial predictions rise steadily before the wind peak. However, the two partial predictions associated with geopotential thicknesses peak before $UV700$ reaches its maximum intensity and quickly drop after: $UV700$ is only maintained by $Z300$ after its peak. The asymmetry between $Z300$ and dZa_UP can be investigated with Figures 3 and 4. Focusing on Figure 3-A, two days before the wind peak, a gradient in geopotential is already present over the UIB in relation to the positive geopotential anomaly ahead of the WD (increasing $Z300$). This gradient is indicative of a southerly advection and a warm anomaly that limits the presence of any gradient in temperature (increasing dZa_UP). At the wind peak (Figure 3-B), the approaching WD tightens the gradient of the 300 hPa geopotential while the colder air remains at the edge of the UIB (peak of both $Z300$ and dZa_UP contributions). Two days after the wind peak at 700 hPa (Figure 3-C), the WD enters the UIB with its cold core. The geopotential gradient remains tight, but the increased temperature gradient counterbalances it, so that the southerly wind at 700 hPa weaken ($Z300$ remains high but dZa_UP quickly decrease).
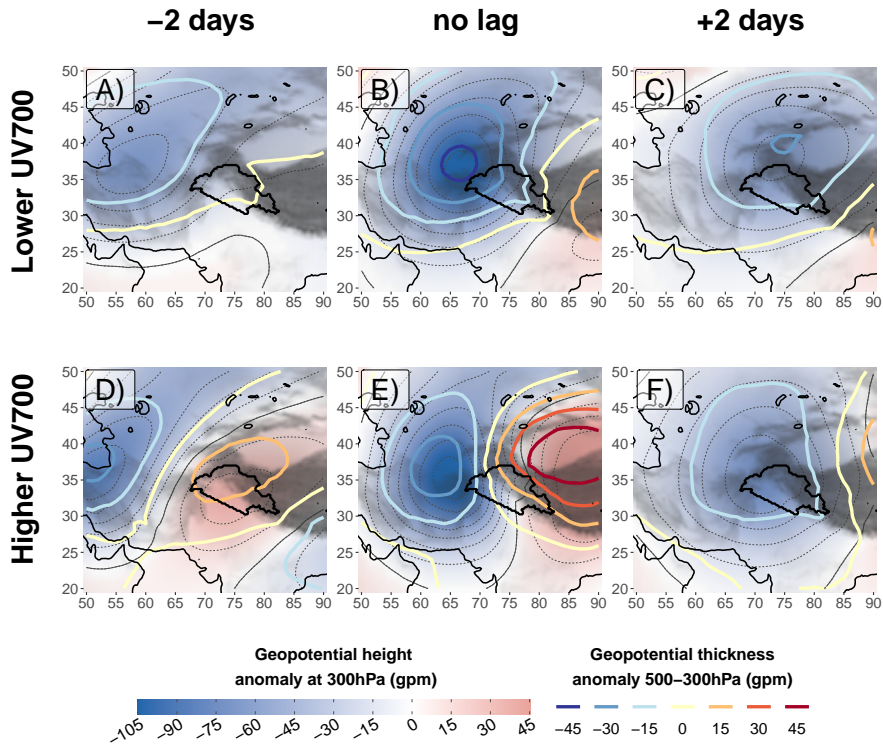
Figure 8. Same as Figure 3, but the composites are based on a subsampling of lower (higher) values of $UV700$, while still above the 90th percentile, in panels A to C (D to F). The subsampling is made so that it is not impacted by seasonality nor by the intensity of the WD (see Section 3.3). This way, comparisons can be made with Figure 3.

4.3 Geostrophic processes and baroclinic interaction

4.3.1 Importance of the upper-troposphere geopotential gradient

The PC regression indicates that the presence of an east-west geopotential gradient across the UIB is more important × Figure 6-B). The importance of this gradient is confirmed by the presence of a positive geopotential anomaly over the Tibetan Plateau during high $UV700$ events (Figure 3-B). The intensity of this anomaly is also clearly coupled with that of $UV700$ (Figure 8-B and E).

This anticyclonic anomaly is already present over the UIB two days before the wind peak (Figure 3-A) and in conjunction with the WD forms a wave train that is already discussed in the literature (Dimri, 2013; Hunt et al., 2018b). However, these previous studies have not stressed the importance of this anticyclonic extreme, which increases the zonal gradient of geopotential to the east of the WD and thus strengthens the southerly wind. The downward propagation of that gradient of pressure is sufficient to trigger the cross-barrier meridional flow. In fact, the zonal gradient is already present at $700\,\mathrm{hPa}$ one day before the wind peak, despite the mean WD centre located at about $1500\,\mathrm{km}$ to the west, owing to the tilt of the circulation and the

presence of positive geopotential anomalies towards the Himalayas. Hence, cross-barrier wind and precipitation can all occur well ahead of a WD. By contrast, when the WD is above the UIB, the zonal gradient of geopotential at $700\,\mathrm{hPa}$ disappears, stopping the cross-barrier meridional flow (Figure 4-C and F).

4.3.2 Changes in WD motion speed

The speed of the mean WD can be calculated using the lead/lag analysis: the centre moves by $13°$ of longitude in two days between Figure 3-A and Figure 3-B, indicating a mean speed of about $6.8\,\mathrm{m\,s^{-1}}$, which is not far from the phase velocity of $5\,\mathrm{m\,s^{-1}}$ found in Hunt et al. (2018b), but is slower than the 8 to $10°$ per day found in Datta and Gupta (1967) (see Dimri et al., 2015). Interestingly, Figure 3-C shows a slowing of the mean WD to about $3.1\,\mathrm{m\,s^{-1}}$, although the composite method limits the analysis in terms of mean speed of the WDs. Slower or even static cyclonic circulation on the surface is sometimes discussed in the literature (e.g. Lang and Barros, 2004; Dimri and Chevuturi, 2014), but not the slowing of the tropopause disturbance itself.

The speed of the WD is also different whether higher or lower $UV700$ is considered (Figure 8). Before the peak of $UV700$, the WD is moving significantly faster in the group with the highest peak values of $UV700$ ($6.8\,\mathrm{m\,s^{-1}}$, Figure 8-D and E) than in the other group ($4.2\,\mathrm{m\,s^{-1}}$, Figure 8-A and B). This change in translation speed does not seem to be related to a change in the $250\,\mathrm{hPa}$ wind speed (Figure 9). We rather suggest it to be related to a difference in the mechanisms explaining the development of the wave supporting the WD.

In the lower $UV700$ case, the development of the WD is accompanied by the reinforcement of the cold anomaly (Figure 8-A and B), suggesting that the tropopause anomaly mostly grows from the equatorward motion of cold air at the rear of the WD. This growing process results in a steady upwind propagation of the wave. By contrast, the temperature anomaly does not change as the WD with higher $UV700$ approaches the UIB and strengthens (Figure 8-D and E). In this case, the WD doesn't grow, but propagates faster.

Furthermore, a stronger cross-barrier wind results in a more severe slowing of the WD. After the peak of $UV700$, the WD with higher $UV700$ slows to $3.2\,\mathrm{m\,s^{-1}}$ (Figure 8-E and F), even slower than the WD with lower $UV700$ ($3.8\,\mathrm{m\,s^{-1}}$, Figure 8-B and C). The intensifying uplift in the UIB during a high cross-barrier wind event increases the near tropopause convergence over the UIB (cf. Quadrupole on divergence field in Hunt et al. 2018a). This convergence zone results in the decay of the WD from its east, and therefore the WD's slowing. This process corresponds to the last and decaying stage of a baroclinic interaction which is now further investigated.

4.3.3 Thermal structure feedback

A first simple way to describe the baroclinic interaction at play in the UIB is through the feedback between circulation and thermal structure. The analysis of the PC regression reveals the importance of the horizontal temperature gradient at $300\,\mathrm{hPa}$ and how a displaced or weaker cold core enhances the circulation at $700\,\mathrm{hPa}$. Yet, the southerly wind east of the WD brings warm air to the Indus plain at all altitudes (Figure 4), depending on the large scale north-south temperature gradient. This flow therefore contributes to displacing the cold core of the WD to the west of its circulation centre at the tropopause, and to
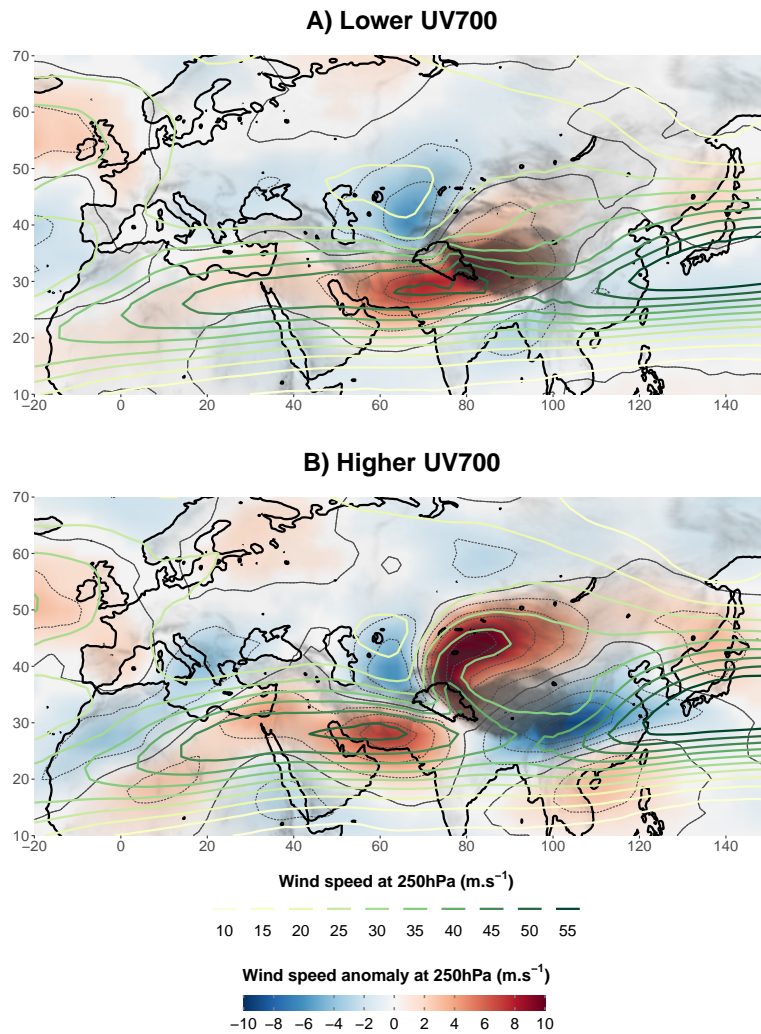
Figure 9. Same fields as in Figure 5-C, but for composites based on the same selections as in Figure 8-B and E.

reinforcing the $700\,\text{hPa}$ circulation in the Indus. The Iranian plateau and the Hindu Kush act as a barrier to the arrival of the cold air from the north-west, while the flat Indus plain channels the southerly wind, further enhancing the positive feedback process.

At local scale, the UIB is a hotspot where most of the near surface convergence occurs. There, warm advection, latent heat release, and mixing prevents the cold air from extending into the UIB as the WD progresses eastwards. The tropospheric zonal temperature gradient is therefore reduced, which in turn increases the geopotential height gradient at $700\,\text{hPa}$ and thus the cross-barrier wind and the uplift (see analysis of the PC regression). This effect explains the general potential for intense

cross-barrier winds in the area. The cold core eventually enters the UIB when the cold air invades the Indus plains to the the South of the UIB and stops the advection of warm air.

4.3.4 Ageostrophic circulation induced by baorclinicity

355   Baroclinic interaction can also be described using quasi-geostrophic theory and potential vorticity (PV). When a positive PV anomaly evolves in a sheared environment, baroclinically forced vertical velocities occur: uplift upwind of the anomaly, and subsidence downwind (Malardel, 2005). More specifically, it is the zonal gradient of PV ahead of (behind) the PV anomaly that triggers the baroclinic uplift (subsidence). A baroclinic interaction occurs when a surface and a tropopause anomaly align such that the vertical velocities associated with one enhances the other anomaly by stretching it. The two disturbances grow

360   and their associated vertical velocities increase until the shear leads to the spatial dephasing of the disturbances. Then, a reverse negative feedback process takes place, leading to the quick decay of both disturbances. These processes characterise the most intense cyclonic activity (Malardel, 2005; Dacre et al., 2012)

     A WD is characterised by a high PV anomaly (Hunt et al., 2018a), and the SWJ in which it is embedded provides the shear needed to produce the vertical velocities. This process has already been suggested as a key factor for explaining vertical

365   velocities in the UIB (Sankar and Babu, 2020) or the interaction with tropical depressions (Hunt et al., 2021). However, as discussed earlier (Section 4.1.1), there is no evidence of a near surface disturbance that would trigger a baroclinic interaction. This has lead Hunt et al. (2018a) to describe WDs as "immature baroclinic waves". We further suggest that the relief and the orographic uplift provides the low altitude feedbacks for a similar, yet short lived, baroclinic interaction.

     The zonal gradient of PV upwind of the WD triggers a baroclinic uplift to the east of the anomaly. As the WD approaches

370   the UIB, its interaction with the relief results in an orographic uplift, which combines with the baroclinic uplift. However, the uplift also results in decreased PV at high altitude ($300\,\mathrm{hPa}$) over the UIB due to the advection of lower tropospheric PV as well as diabatic heating. Hence, the zonal PV gradient increases and stronger baroclinic uplift occurs, resulting in a positive feedback. Once the high PV anomaly associated with the WD enters the UIB, the mechanism reverses: the orographic uplift results in the weakening of the PV anomaly, eventually leading to the decay of the WD.

375   The input of low PV at high altitude from the UIB is evident from the anticyclonic turn of the outflow (seediscussion on Figure 5-C, in section 4.1.3) and from the warm area at $300\,\mathrm{hPa}$ to the east of the WD but largely displaced compared to the geopotential anomaly maximum (Figure 3-B). Moreover, the baroclinic interaction and the intense uplift is revealed by the deformation of the jet near the UIB during the passing of the WD (Figure 5). Particularly, when the uplift is maximum, the jet configuration is characteristic of a strong divergence at the tropopause over the UIB: the study area is located near the eastern

380   exit of the Arabian Jet, and in the right entrance of the outflow[5]. This mechanism is similar to the baroclinic interaction between a tropopause anomaly and a surface disturbance, but where the surface disturbance is replaced by the relief. It also results in a weaker, shorter-lived interaction.

---

[5]On a jet streak, the right entrance and the left exit are characterised by baroclinic convergence at the tropopause and tropospheric uplift (Malardel, 2005)

The different thermal structures shown in Figure 8 are linked to a difference in the strength of baroclinic processes. This difference becomes evident when looking at the wind at $250\,\text{hPa}$. In case of higher UV700 (Figure 9-B), the pattern of wind anomaly is very similar to Figure 5-C. The outflow is more intense and clearly detached from the anomalously strong SWJ. By contrast, in case of lower $UV700$ (Figure 9-A), the anomalously strong SWJ extents to the South-East of the UIB and forms a diffluence over the Tibetan Plateau, while there is no evidence of a distinct outflow. In that context, the UIB is not any more located in a tropopause divergence configuration.

To conclude, WDs are a prerequisite to cross-barrier barrier winds in the UIB. Both the strength of the $300\,\text{hPa}$ low and its baroclinic context are important for the cross-barrier wind intensity. In the composites in Figure 8, $UV700$ is 2/3 higher in the higher case ($5.3\,\text{m}\,\text{s}^{-1}$) than in the lower case ($3.2\,\text{m}\,\text{s}^{-1}$), a difference mostly explained by the difference in baroclinicity. However, the increase in precipitation is almost 3 fold, from $5.9\,\text{mm}\cdot\text{3hrs}^{-1}$ to $16.8\,\text{mm}\cdot\text{3hrs}^{-1}$. This difference is partially explained by the quadratic fit (seeFigure 2-B), but also by a change in moisture supply ($Q700$), from $3\times10^{-3}\,\text{kg}\,\text{kg}^{-1}$ to $3.6\times10^{-3}\,\text{kg}\,\text{kg}^{-1}$, which is now further investigated.

5 Relating moisture contribution variability to Western Disturbances

5.1 General

The UIB and the Indus Plain are dominated by a mean westerly moisture flux during the season of active WDs (Figure 10-A). However, precipitable water is over 15mm in the Indus Plain, while it is below $10\,\text{mm}$ to the west of the plain, in relation to the higher elevations (e.g. Suleiman range, Hindu Kush, Iranian plateau). This being the case, transient circulation or local evaporation are needed to explain the higher amount in the plain. Furthermore, the moisture content (and moisture contribution, $Q700$) rises during a peak of $UV700$ and in the days before as shown in Figures 4-D and E, and 7, indicating the importance of WDs in moisture variability. Therefore, to understand the origin, pathway and variability of the moisture that eventually precipitates, the moisture flux needs to be investigated during the passing of a WD.

5.2 Moisture pathway to the UIB

Figure 10-E shows a significant accumulation of precipitable water in the UIB when $UV700$ is maximum: the anomaly represents an increase of 30 to 50% in precipitable water in the UIB compared to the mean. The anomaly extends along the Himalayas, towards northeast India, as well as towards the Arabian Sea. Hunt et al. (2018b) found a similar pattern when investigating extreme precipitation events. This relationship between wind and precipitable water is first explained by the near surface moisture convergence induced by the cross-barrier wind, particularly near the foothills. However, composites of negative lags in Figure 10-B, C, and D suggest that anomalously wet air masses advected into the UIB are also responsible for the increase in precipitable water.

Four days before the peak of $UV700$, moisture is already building up over the Persian Gulf (Figure 10-B). The direction of moisture transport indicates that this moisture is advected from the Red Sea across the Arabian Peninsula. This transport,
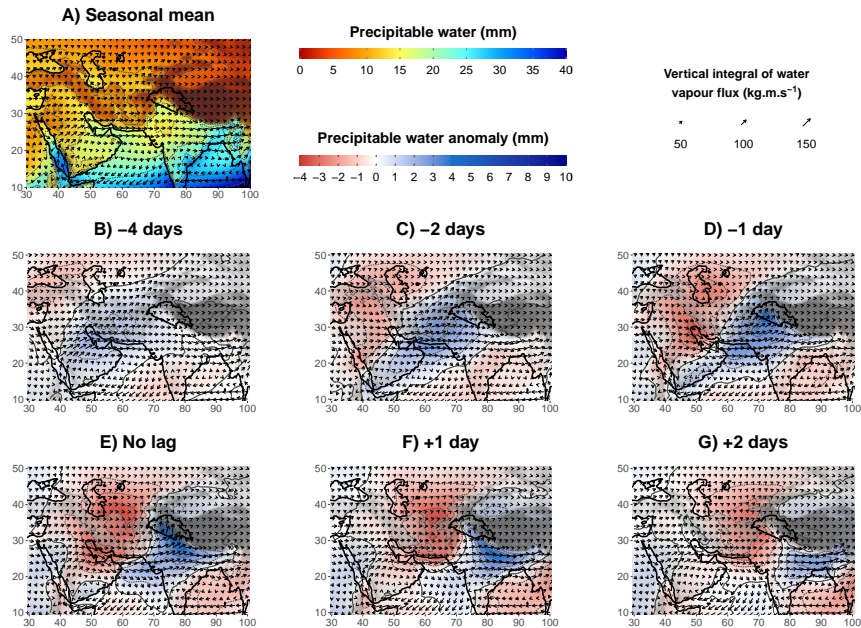
Figure 10. In Panel A, Seasonal mean of precipitable water (colour shading, thin contour lines every 5mm) and vertical integral of water vapour flux (arrows). The mean is weighted by the seasonality of occurrence of $UV700$ above its 90th percentile. Panels B to G show the lead/lag composite maps, with respect to the 10% highest values of $UV700$ (as in Figure 3), of precipitable water anomaly (colour shading, thin contour lines every $2\,mm$) and absolute water vapour flux (arrow). Non-significant anomalies at the level 95% are shown in white.

and how it is enhanced by Mediterranean lows, is described in Chakraborty et al. (2006) and Mujumdar (2006). This moisture
415 flow passes over the coastal mountain ranges along the Red Sea (Sarawat Mountains, with peak heights ranging from 1000 to $3000\,m$). The moisture is therefore present at a relatively high altitude, similar to that of the cross-barrier wind in the UIB ($700\,hPa$). The more intense wind at this altitude than closer to the surface has the potential to quickly transport the moisture towards the study area.

Two days later (Figure 10-D), the positive anomaly of precipitable water has spread from the north side of the Arabian Sea to
420 the Indus Plain and the mountains to the west. The south-westerly moisture flux clearly suggests that air masses from the north of the Arabian Sea and the Persian Gulf contribute to the increase in precipitable water, as mentioned by Hunt et al. (2018b). Moisture convergence over the windward side of the mountains also helps to increase moisture at higher altitudes as can be seen over the Suleiman Range, one day before the peak in Figure 4-D. Convergence also starts over the UIB, more specifically in the notch formed by the mountain ranges, one day before the peak of $UV700$, resulting in a maxima of precipitable water
425 anomaly (Figure 10-D).

This analysis shows the existence of a pathway of moisture that sustains moisture content in the UIB. It originates from the Red Sea, crosses the Arabian Peninsula towards the Persian Gulf, continues towards the north of the Arabian Sea, the Indus Plain and ends in the UIB. Previous studies have implied the existence of such a pathway without investigating it further (Filippi et al., 2014; Hunt et al., 2018b; Ahmed et al., 2019). Part of this circulation, from the Red Sea to the Arabian Sea, is visible in the seasonal mean (Figure 10-A) and is driven by the subtropical gyre located on the southeastern tip of the Arabian Peninsula. WDs strengthen this flow as suggested in Hunt and Dimri (2021) but most importantly steers it towards the UIB. In some extreme cases, this moisture pathway can form atmospheric rivers (cf. Bao et al., 2006; Zhu and Newell, 1998) that are related to extreme precipitation events along the Himalayas (Thapa et al., 2018). This analysis also suggests that neither the Mediterranean Sea nor the Caspian Sea are important contributors of moisture for the precipitation in the UIB, in agreement with Jeelani et al. (2018); Dar et al. (2021).

5.3 Evaporation sources

The local evaporation in the UIB is quite high compared to the surrounding land, about 1 to $2\,\text{mm}$ per day (Figure 11-A) and is little affected by the passing of a WD (Figure 11-C). While this process helps sustain the generally higher precipitable water in the UIB, it cannot explain the precipitable water anomaly associated with a WD. The rest of the Indus Plain, or the nearby mountains, contribute very little to the moisture, as those areas are arid, and the wetter and higher ground is too cold in winter to generate significant evaporation.

The mean evaporation rate over the Persian Gulf and the north Arabian Sea is about 4 to $5\,\text{mm}$ per day (Figure 10-A). That is, a day of evaporation represents the quarter of the total precipitable water in the area. This high replacement rate suggests that a large amount of the moisture arises from those water bodies directly, and it also emphasizes the importance of the persistence of the moisture pathway between the two to build up moisture content. Even stronger evaporation rates are present in the Red Sea, particularly to the north. As mentioned earlier, despite the distance, the Red Sea seams important for increasing moisture at higher altitudes, so that it can be more easily transported.

These two composite analyses clearly identify the north of the Arabian Sea, the Persian Gulf, and the Red Sea as the main sources of moisture for the precipitation in the UIB for the first time. However, this approach does not allow for any quantification, nor does it discuss variability. A more complex analysis involving numerical tracking would be needed, and that is beyond the scope of this study.

5.4 Other impacts of the passing of WDs on the moisture field

WDs impact the intensity and end point of the moisture pathway (Section 5.2), but other impacts are evident from Figure 10 and 11 as well. Two days before the peak of $UV700$, a negative anomaly of precipitable water propagates from Tigress-Euphrates plain into the Persian Gulf (Figure 10-C), and reduces the moisture supply from the Red Sea. This circulation is the result of a surge of a surface, cold, and dry air at the rear of WDs. The negative anomaly eventually propagates to the north of the Arabian Sea after the peak of $UV700$ (Figure 10-E, F, and G), but tends to weaken. This weakening can be explained by the large evaporation anomaly present over the seas as the dry air progresses (Figure 11-B, C, and D). Evaporation rates almost
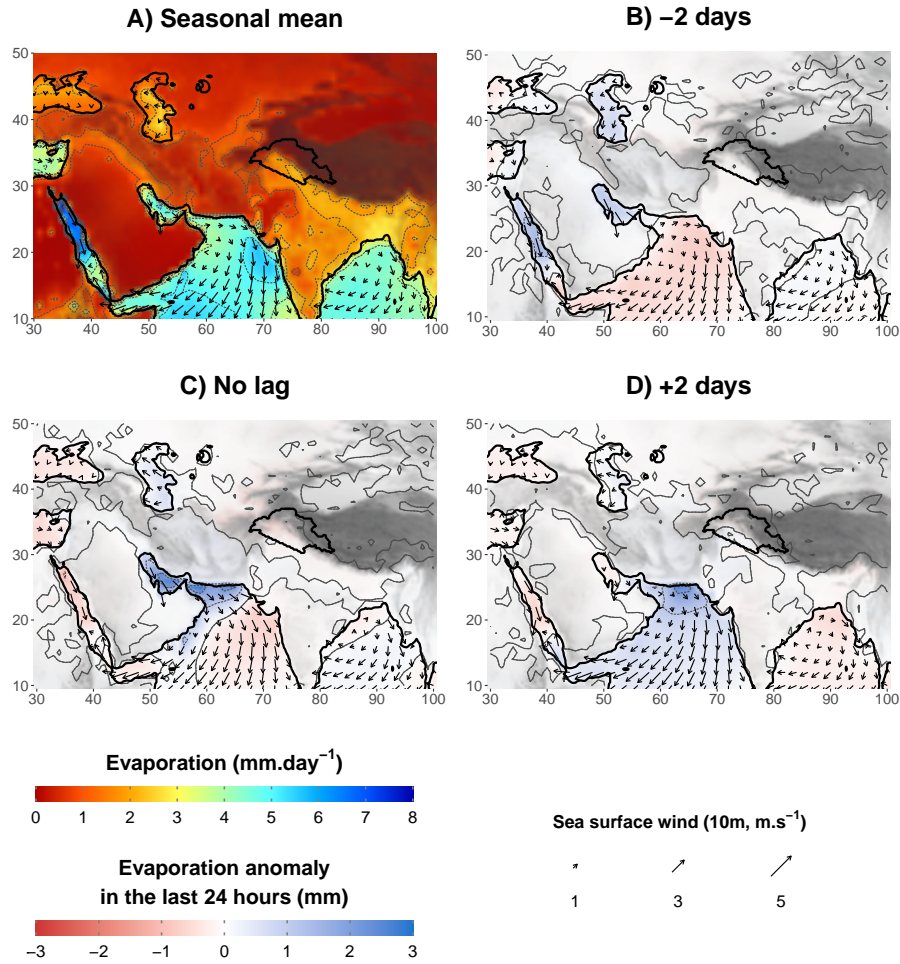
Figure 11. Panel A is similar to Figure 10-A but for evaporation (colour shading, thin contour lines every $5\,\mathrm{mm}$) and 10m sea winds (arrows). Panels B to D are similar to Figure 10-C, E and G but for cumulated evaporation in the last 24 hours before the peak of $UV700$ plus the lead or lag indicated (colour shading, thin contour lines every $2\,\mathrm{mm}$) and 10m sea winds (arrows).

double compared to the seasonal mean (Figure 11-A), which is enough to eliminate the precipitable water anomaly in a day.

460 This evaporation anomaly can be explained by both the increase in surface wind speed induced by the WD (arrows on Figure 11) and the very low surface dew point of the air blown from the land.

A second but connected area of negative anomaly of precipitable water is present over Central Asia and the Caspian Sea (Figure 10-C and D). It also relates to cold and dry air being advected by the WD from northern latitudes. When $UV700$ peaks, this cold and dry air mass invades the mountains to the west of the Indus Plain (Figure 10-E, see also Figure 4-B and D). Unlike

465 the other air masses that are advected over the sea, the encounter with the relief further increases the moisture anomaly through a Foehn effect. This effect is strongest after the peak of $UV700$, as the mean moisture flux over the Indus Plain veers eastward.

The continental dry air descends from the Suleiman Range and the Hindu Kush, replacing the maritime moist air (Figure 10-F and G). As the UIB is cut from its moisture supply, the precipitable water anomaly becomes negative (Figure 10-G), which severely limits moisture transport and precipitation despite the continued presence of a cross-barrier wind. Similarly, Figure 7 indicates that the passing of a WD noticeably reduces $Q700$ several days after the peak of $UV700$.

Hence, a WD has two opposite effects on moisture content in the UIB: moistening before its passing, and drying afterwards. Therefore, another ensuing WD may be inhibited, in terms of precipitation, by the dryer conditions dominating in the Indus Plain and the UIB, suggesting a negative feedback effect. However, one could also imagine a positive feedback, where a quick succession of WDs provides a continuous moisture supply from the maritime sources by inhibiting the dry air invasion. The interaction between WDs is not further investigated here and is likely subject to high variability and dependent on larger and smaller-scale atmospheric circulation.

After the peak of $UV700$, the positive anomaly of precipitable water moves along the Himalayas towards northeast India where it enhances cross-barrier moisture transport and orographic precipitation in another notch that is formed by the relief, enhancing orographic precipitation there. The impact of WDs is not as evident in this area, first because the tropopause distur-bances have mostly disappeared due to the interaction with the relief in the UIB, and because convection is a more important driver of precipitation (Tinmaker and Ali, 2012; Mahanta et al., 2013; Mannan et al., 2017).

Finally, the north-easterly trade winds that blow over most of the Arabian Sea are also affected by WDs: they are weaker ahead of the WD, leading to a decreased evaporation (Figure 11-B), which also slightly decreases precipitable water along 10°N (Figure 10-B to E). However, trade winds intensify after the passing of the WD, thus increasing evaporation (Figure 11-D) and leading to a slight increase in precipitable water to the south (Figure 10-F and G).

5.5 Impact of WD characteristics on $Q700$

Various WDs characteristics influence moisture contribution ($Q700$). There exists a direct link between $UV700$ and $Q700$: their peak is concurrent as a WD passes (Figure 7), and their correlation reaches 0.45 for the entire winter season (once the seasonal mean is removed from $Q700$). This relationship is explained by the advection of moisture by the cross-barrier wind from both the south (from the moisture pathway) and the near surface (due to uplifting). Since the intensity and the thermal structure of a WD at $300\,\mathrm{hPa}$ impact $UV700$ (seeSection 4.2), they also impact $Q700$. However, the shape and direction of a WD has an even greater impact by acting on the balance between the supply of maritime moist air and the intrusion of continental dry air discussed earlier (Section 5.4). This impact is investigated using the results of the second quantile regression described in Section 3.3, and composite maps over two selections, one representative of low $Q700$ and the other of high $Q700$ (Figures 12 and 13).

As expected, the two selections exhibit very different patterns of precipitable water anomaly when $UV700$ is maximum (Figure 12-E and F). In case of high $Q700$, a high positive anomaly is present from the Arabian Sea to northeast India, with a maximum over the UIB, indicating a sustained supply of moisture. By contrast, a negative anomaly is present over the Indus Plain in the case of low $Q700$, showing that continental dry air is already invading the plain, cutting off any potential moisture
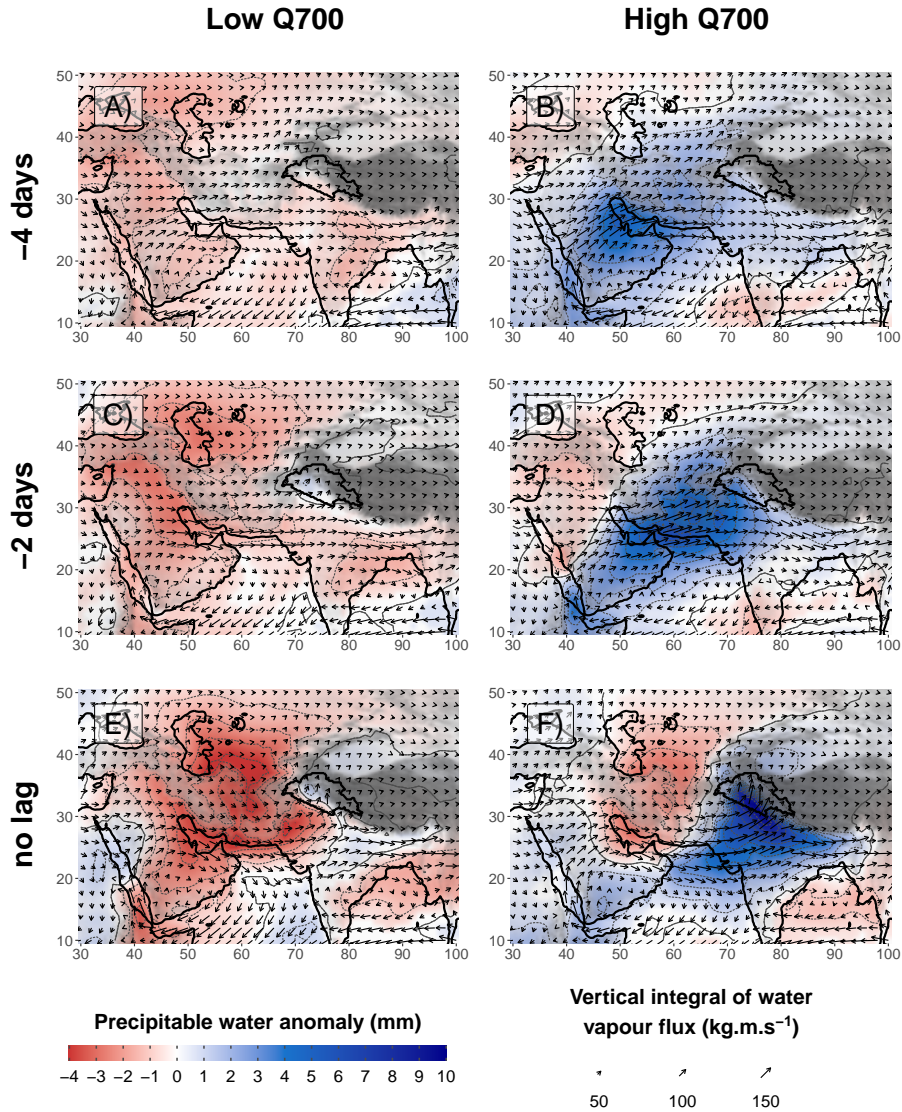
Figure 12. Same as Figure 10 (B, C and E), but the composites are based on the lowest (highest) values of $Q700$ in panels A, C, and E (B, D and F). See the selection definition in Section 3.3.

supply from the moisture pathway. A small positive anomaly remains in the UIB, probably thanks to the uplifting. Interestingly, no evident difference in moisture flux direction is visible between the two panels (Figure 12-E and F).

The explanation of the differences in moisture content lies in the circulation history. In case of high $Q700$, moisture over the Persian Gulf increases more than in the average case four days before the peak of $UV700$ (Figures 10-B and 12-B), due to stronger moisture transport across the Arabian Peninsula. This moisture anomaly moves towards the Indus Plain, the mountain ranges to the west, and even towards parts of Central Asia two days later (Figure 12-D), pushed by a strong southerly

	–2 days	no lag
Low Q700	A)	B)
High Q700	C)	D)

Geopotential height anomaly at 300hPa (m².s⁻²)

Geopotential thickness anomaly 500–300hPa (m².s⁻²)
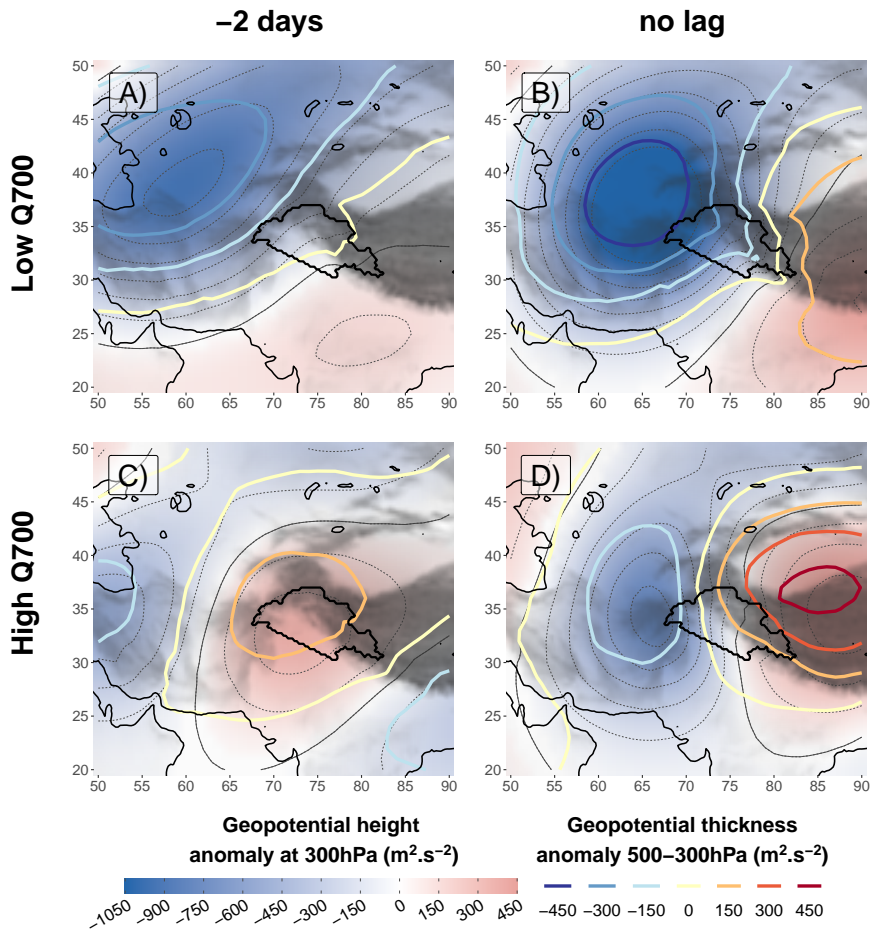
Figure 13. Same fields as Figure 3, but for composites based on the same selections as in Figure 12-C to F.

component of the moisture flux. The larger extent of the precipitable water anomaly than in the average case (Figure 10-C) effectively delays the intrusion of continental dry air (Figures 12-F and 10-E). In the low $Q700$ case, no such positive anomaly is present (Figure 12-A and C): the WD is not accompanied by a strengthening of the moisture pathway, and the southerly component of the moisture flux is almost absent. Instead, negative anomalies of precipitable water build up over Tigress-

510 Euphrates plain and Central Asia (Figure 12-C) and move eastward and south-eastward respectively towards the Indus Plain (Figure 12-C). These patterns show that the balance between moisture advection ahead of a WD and dry air intrusion at the rear may vary significantly.

This difference in moisture flux can be explained by the origins and tracks of WDs. In case of high Q700, the mean low at $300\,\mathrm{hPa}$ exhibits an eastward motion around 33-34° N, which is slightly more to the south than the general case (36° N). The

515 WD also exhibits a weaker cold core, and a larger zonal gradient of geopotential to its east than in the general case (Figures 3-B and 13-D), implying a stronger southerly wind at 700 hPa. Both southern location and stronger southerly advection at $700\,\mathrm{hPa}$

explains how these WDs are able to draw more moisture from the sub-tropical latitudes along their path. Furthermore, stronger mid-tropospheric warm advection and latent heat release over the mountains to the west of the UIB, due to the higher moisture content, can enhance the wind circulation at $700\,\mathrm{hPa}$ so that $UV700$ remains higher than in the general case ($4.4\,\mathrm{m\,s^{-1}}$ instead of 4.1) despite the weaker geopotential anomaly at $300\,\mathrm{hPa}$ (Figure 13-B and D).

By contrast, in case of low $Q700$, the mean WD originates from the north-west, towards the Caspian Sea, which means it interacts less with the moisture pathway. The WD is also characterised by a deep cold core, which, despite a stronger geopotential anomaly, results in a lower $UV700$ than in the general case ($3.8\,\mathrm{m\,s^{-1}}$). The WDs are also much slower than in the general case ($3.3\,\mathrm{m\,s^{-1}}$), and, as for the case of lower $UV700$ discussed in Section 4.3.2, we suggest that this is due to the equatorward motion of cold air at the rear of the WD, which is reinforced here by the originally more northern position of the WD. A different way to explain the growing of the WD is through its position relative to the SWJ. The SWJ produces a jet streak to the south-east of the WD. Consequently, such a WD is located on the left entrance of the jet, where convergence and subsidence are enhanced. Therefore, the WD can grow by stretching its vorticity, while the surface cyclonic circulation and the convergence at $700\,\mathrm{hPa}$ is reduced. In the meantime, the subsidence leads to a further drying of the atmosphere.

Finally, moisture transport from the trade winds in the Arabian Sea also vary between the two selections: it is stronger (weaker) in case of lower (higher) $Q700$, regardless of the position of the WD (arrows, Figure 12). We discussed with Figure 10 how trade winds are impacted by the passing of a WD, but trade winds can also impact the moisture field outside of the WD influence. In particular, stronger trade winds transport the moisture evaporating from the Arabian Sea to the Southern Hemisphere, while weaker trade winds allow for a build-up of moisture. Hence, moisture supply to the UIB is also coupled to the tropical and sub-tropical variability.

6 Summary

This study has developed an in-depth analysis of the synoptic variability of precipitation in the Upper Indus Basin (UIB) during winter using PC regressions, quantile regressions and composites, furthering methods developed in Baudouin et al. (2020a). Several processes explaining WD growth, decay, interaction with the relief, and relationship with precipitation are suggested. In particular, the atmospheric circulation related to precipitation has been discussed and is summarised in Figure 14.

Precipitation in the UIB (in yellow, 1) is related to the arrival of an upper troposphere disturbance from the west (Western Disturbances, 2). This disturbance is embedded in the Subtropical Westerly Jet, which forms to the west a local maxima, the Arabian Jet (3). The upper disturbance grows in part from the equatorward advection of cold air through baroclinic processes (4). This cold air is funnelled between an anticyclonic anomaly and a trough (5) and is responsible for the strengthening the Arabian Jet (3). The cold air advection has an ambivalent role as it is accompanied by dry air close to the surface that can suppress precipitation (6).

Winter moisture transport is driven by the Arabian subtropical high (7). North of it, a westerly moisture pathway (8) connects the Red Sea with the Persian Gulf and the north of the Arabian Sea, while trade winds (9) blow over the rest of the Arabian Sea. The passing of a WD enhances the westerly moisture pathway (8), while it weakens trade winds (9). As the WD approaches
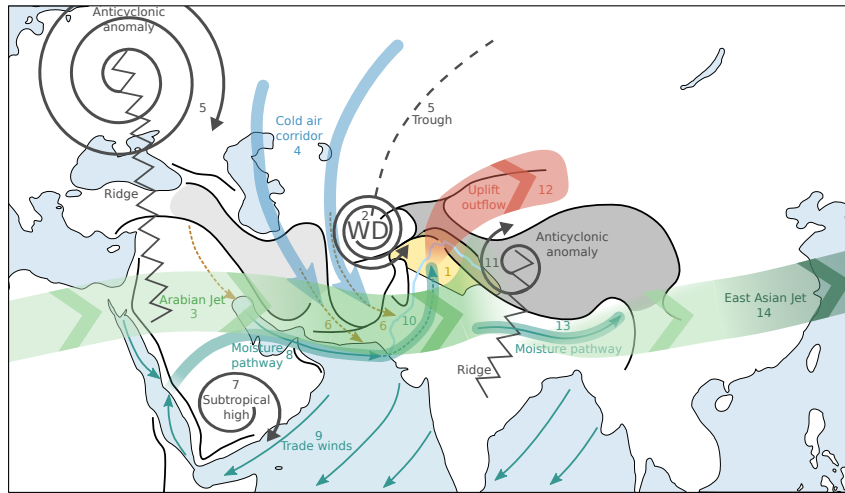
Figure 14. Sketch summarising the atmospheric circulation when a WD interacts with the relief to produce precipitation in the UIB. The UIB is in yellow, and the Indus River in pale blue. The black lines indicate major mountain ranges, and the grey-shaded areas high plateaus (The Tibetan Plateau and the Iranian Plateau). The spirals represent tropospheric geopotential anomalies or centres of actions. The thin sea-green arrows are mean lower troposphere moisture transport. A thicker accent indicates higher altitude transport, and a dotted line indicates transient transport due to the WD. The brown dotted lines indicate advection of dry air by the WD near the surface. The blue arrows are troposphere wide cold air advections. The thick green arrows represent the upper troposphere jets, with darker colour indicating stronger winds. The red arrow relates to the warm upper troposphere outflow. Finally, the numbers are in-text references.

550   the UIB, it steers the moisture across the Indus Plain into the notch formed by the relief (10). The presence of an anticyclonic anomaly east of the WD further enhances the meridional transport (11). This advection of warm and moist air sustains itself, in particular its component close to the surface, through baroclinic and latent heat feedbacks at the synoptic scale.

Eventually, the moisture converges at low-level (around $700\,\mathrm{hPa}$) in the UIB, over the foothills, where the uplift triggers condensation and precipitation (1). It also allows for a mixing and a warming of the air column in the UIB, which counter-

555   balances the cold air advection associated with the WD (4). In other words, the uplift advects low potential vorticity values to high altitude ($250\,\mathrm{hPa}$) as indicated by the swift anticyclonic turn of its outflow (12), which then increases the zonal gradient of potential vorticity. Consequently, the upper troposphere cyclonic circulation of the WD further propagates downward, while the baroclinic uplift and the cross-barrier moisture transport increases (10). The increased vertical velocities and high altitude convergence lead to a break in the Arabian jet (3).

560   This positive baroclinic interaction, however, is short-lived. Once the WD reaches the UIB, its high PV anomaly is consumed by the continued advection of low PV, which quickly leads to the weakening of the cyclonic circulation. Furthermore, in addition to this negative baroclinic feedback, dry continental air intrudes into the Indus Plain (6) and cuts off the moisture supply to the UIB, which effectively further suppresses precipitation. The remaining moisture surplus is then pushed towards

northeast India (13), while trade winds in the Arabian Sea re-intensify (9). Finally, as the result of the WD interaction with the relief, the Subtropical Westerly Jet weakens to the east of the UIB and this negative anomaly propagates along the East Asian Jet in the following days (14).

Winter precipitation and cross-barrier wind in the UIB is unequivocally related to the passing of Western Disturbances close to the tropopause. However, the idealised scenario presented in Figure 14 hides large variability in the different features discussed. On the one hand, a PC regression demonstrated that cross-barrier wind is not only affected by how deep the upper geopotential anomaly of the WD is but also by the geopotential gradient east of the WD and by the position and intensity of the cold core of the WD. These characteristics could be used to explain why some WDs trigger very little precipitation. On the other hand, a quantile regression showed that the build up of moisture in the UIB is dependent on the history of the WD's development and track. The importance of these effects is reinforced by the approximately quadratic relationship that exists between precipitation and cross-barrier moisture transport at 700 hPa and between cross-barrier wind and WD characteristics. The latter may also be related to non quasi-geostrophic and meso-scale effects, potentially unrelated to WDs (e.g. convection or frontal activity), which haven't been explored here but could constitute a topic for future investigations. Other topics whose analyses can build upon the methods and results presented here include the origin of Western Disturbances and their relation to anticyclonic anomalies over Eastern Europe, the seasonal cycle of precipitation, and its intra-seasonal and inter-annual variability, all of which have been only partially addressed in (e.g. Baudouin, 2020).

Code availability. The code in R used to produce the figures is available at https://doi.org/10.5281/zenodo.5115561

Author contributions. Original idea, analysis and text by JPB, guidance and review by MH and CP

Competing interests. The authors declare that they have no conflict of interest

Disclaimer. This paper consists in large part of the Chapter 4 of the thesis of Jean-Philippe Baudouin, submitted for the degree of Doctor of Philosophy at the University of Cambridge (https://doi.org/10.17863/CAM.68377).

Acknowledgements. We first acknowledge the ECMWF teams in charge of producing the ERA5 reanalysis and sustaining the online availability of the datasets. We also acknowledge our editor and our reviewers (to be precised).

JPB thanks the two examiners of his PhD dissertation, Andrew G. Turner and Andrew N. Ross, for their constructive discussions that helped shaping this paper. JPB also personally thanks Kira Rehfeld, the STACY group, and the *PalMod-Phase 2* project funded by the German Federal Ministry of Education and Research (BMBF), for their support towards the completion of his PhD.

590   This research was carried out as part of the *TwoRains* project, which is supported by funding from the European Research Council (ERC) under the European Union's Horizon 2020 research and innovation programme.

For the financial support section: ERC grant agreement no. 648609, and BMBF grant no. 01LP1926C

References

Agnihotri, C. and Singh, M.: Satellite study of western disturbances, Mausam, 33, 249–254, 1982.

Ahmed, F., Adnan, S., and Latif, M.: Impact of jet stream and associated mechanisms on winter precipitation in Pakistan, Meteorology and Atmospheric Physics, 132, 225–238, https://doi.org/10.1007/s00703-019-00683-8, 2019.

Bao, J.-W., Michelson, S. A., Neiman, P. J., Ralph, F. M., and Wilczak, J. M.: Interpretation of Enhanced Integrated Water Vapor Bands Associated with Extratropical Cyclones: Their Formation and Connection to Tropical Moisture, Monthly Weather Review, 134, 1063–1080, https://doi.org/10.1175/MWR3123.1, 2006.

Baudouin, J.-P.: A modelling perspective on precipitation in the Indus River Basin: from synoptic to Holocene variability, Ph.D. thesis, University of Cambridge, 2020.

Baudouin, J.-P., Herzog, M., and Petrie, C. A.: Contribution of Cross-Barrier Moisture Transport to Precipitation in the Upper Indus River Basin, Monthly Weather Review, 148, 2801–2818, https://doi.org/10.1175/MWR-D-19-0384.1, 2020a.

Baudouin, J.-P., Herzog, M., and Petrie, C. A.: Cross-validating precipitation datasets in the Indus River basin, Hydrology and Earth System Sciences, 24, 427–450, https://doi.org/10.5194/hess-24-427-2020, 2020b.

Bollasina, M. and Nigam, S.: Modeling of Regional Hydroclimate Change over the Indian Subcontinent: Impact of the Expanding Thar Desert, Journal of Climate, 24, 3089–3106, https://doi.org/10.1175/2010JCLI3851.1, 2011.

Boschi, R. and Lucarini, V.: Water Pathways for the Hindu-Kush-Himalaya and an Analysis of Three Flood Events, Atmosphere, 10, 489, 2019.

Brent, R. P.: Algorithms for minimization without derivatives, Prentice-Hall, Englewood Cliffs, New Jersey, 1973.

Cannon, F., Carvalho, L. M., Jones, C., and Bookhagen, B.: Multi-annual variations in winter westerly disturbance activity affecting the Himalaya, Climate dynamics, 44, 441–455, https://doi.org/10.1007/s00382-014-2248-8, 2015.

Cannon, F., Carvalho, L. M., Jones, C., and Norris, J.: Winter westerly disturbance dynamics and precipitation in the western Himalaya and Karakoram: a wave-tracking approach, Theoretical and Applied Climatology, 125, 27–44, https://doi.org/10.1007/s00704-015-1489-8, 2016.

Chakraborty, A., Behera, S. K., Mujumdar, M., Ohba, R., and Yamagata, T.: Diagnosis of tropospheric moisture over Saudi Arabia and influences of IOD and ENSO, Monthly Weather Review, 134, 598–617, https://doi.org/10.1175/MWR3085.1, 2006.

Dacre, H. F., Hawcroft, M. K., Stringer, M. A., and Hodges, K. I.: An Extratropical Cyclone Atlas: A Tool for Illustrating Cyclone Structure and Evolution Characteristics, Bulletin of the American Meteorological Society, 93, 1497–1502, https://doi.org/10.1175/BAMS-D-11-00164.1, 2012.

Dahri, Z. H., Moors, E., Ludwig, F., Ahmad, S., Khan, A., Ali, I., and Kabat, P.: Adjustment of measurement errors to reconcile precipitation distribution in the high-altitude Indus basin, International Journal of Climatology, 38, 3842–3860, 2018.

Dar, S. S., Ghosh, P., and Hillaire-Marcel, C.: Convection, terrestrial recycling and oceanic moisture regulate the isotopic composition of precipitation at Srinagar, Kashmir, Journal of Geophysical Research: Atmospheres, 126, e2020JD032 853, 2021.

Datta, R. and Gupta, M.: Synoptic study of the formation and movements of western depressions, Indian J. Meteorol. Geophys, 18, 45–50, 1967.

de Vries, A. J., Feldstein, S. B., Riemer, M., Tyrlis, E., Sprenger, M., Baumgart, M., Fnais, M., and Lelieveld, J.: Dynamics of tropical–extratropical interactions and extreme precipitation events in Saudi Arabia in autumn, winter and spring, Quarterly Journal of the Royal Meteorological Society, 142, 1862–1880, https://doi.org/10.1002/qj.2781, 2016.

630 Dimri, A. and Chevuturi, A.: Model sensitivity analysis study for western disturbances over the Himalayas, Meteorology and Atmospheric Physics, 123, 155–180, 2014.

Dimri, A. P.: Impact of horizontal model resolution and orography on the simulation of a western disturbance and its associated precipitation, Meteorological Applications, 11, 115–127, https://doi.org/10.1017/S1350482704001227, 2004.

Dimri, A. P.: The transport of momentum, sensible heat, potential energy and moisture over the western Himalayas during the winter season,
635 Theoretical and Applied Climatology, 90, 49–63, https://doi.org/10.1007/s00704-006-0274-0, 2007.

Dimri, A. P.: Intraseasonal oscillation associated with the Indian winter monsoon, Journal of Geophysical Research: Atmospheres, 118, 1189–1198, https://doi.org/10.1002/jgrd.50144, 2013.

Dimri, A. P. and Niyogi, D.: Regional climate model application at subgrid scale on Indian winter monsoon over the western Himalayas, International Journal of Climatology, 33, 2185–2205, https://doi.org/10.1002/joc.3584, 2013.

640 Dimri, A. P., Niyogi, D., Barros, A. P., Ridley, J., Mohanty, U. C., Yasunari, T., and Sikka, D. R.: Western Disturbances: A review, Reviews of Geophysics, 53, 225–246, https://doi.org/10.1002/2014RG000460, 2015.

Filippi, L., Palazzi, E., von Hardenberg, J., and Provenzale, A.: Multidecadal variations in the relationship between the NAO and winter precipitation in the Hindu Kush–Karakoram, Journal of Climate, 27, 7890–7902, 2014.

Grams, C. M., Wernli, H., Böttcher, M., Čampa, J., Corsmeier, U., Jones, S. C., Keller, J. H., Lenz, C.-J., and Wiegand, L.: The key
645 role of diabatic processes in modifying the upper-tropospheric wave guide: a North Atlantic case-study, Quarterly Journal of the Royal Meteorological Society, 137, 2174–2193, https://doi.org/10.1002/qj.891, 2011.

Hewitt, K.: Glacier change, concentration, and elevation effects in the karakoram Himalaya, Upper Indus Basin, Mountain Research and Development, 31, 188 – 200, https://doi.org/10.1659/MRD-JOURNAL-D-11-00020.1, 2011.

Hunt, K. M. and Dimri, A.: Synoptic-scale precursors of landslides in the western Himalaya and Karakoram, Science of The Total Envi-
650 ronment, 776, 145 895, https://doi.org/https://doi.org/10.1016/j.scitotenv.2021.145895, 2021.

Hunt, K. M., Turner, A. G., and Shaffrey, L. C.: The evolution, seasonality and impacts of western disturbances, Quarterly Journal of the Royal Meteorological Society, 144, 278–290, 2018a.

Hunt, K. M., Turner, A. G., and Shaffrey, L. C.: Extreme daily rainfall in Pakistan and north India: scale interactions, mechanisms, and precursors, Monthly Weather Review, 146, 1005–1022, 2018b.

655 Hunt, K. M. R., Turner, A. G., and Schiemann, R. K. H.: How interactions between tropical depressions and western disturbances affect heavy precipitation in South Asia, Monthly Weather Review, https://doi.org/10.1175/MWR-D-20-0373.1, 2021.

Jeelani, G., Deshpande, R. D., Galkowski, M., and Rozanski, K.: Isotopic composition of daily precipitation along the southern foothills of the Himalayas: impact of marine and continental sources of atmospheric moisture, Atmospheric Chemistry and Physics, 18, 8789–8805, 2018.

660 Krishnamurti, T. N.: The subtropical jet stream of winter, Journal of Meteorology, 18, 172–191, https://doi.org/10.1175/1520-0469(1961)018<0172:TSJSOW>2.0.CO;2, 1961.

Krishnan, R., Sabin, T. P., Madhura, R. K., Vellore, R. K., Mujumdar, M., Sanjay, J., Nayak, S., and Rajeevan, M.: Non-monsoonal precipitation response over the Western Himalayas to climate change, Climate Dynamics, 52, 4091–4109, https://doi.org/10.1007/s00382-018-4357-2, 2018.

665 Lang, T. J. and Barros, A. P.: Winter storms in the central Himalayas, Journal of the Meteorological Society of Japan. Ser. II, 82, 829–844, 2004.

Madhura, R. K., Krishnan, R., Revadekar, J. V., Mujumdar, M., and Goswami, B. N.: Changes in western disturbances over the Western Himalayas in a warming environment, Climate Dynamics, 44, 1157–1168, https://doi.org/10.1007/s00382-014-2166-9, 2015.

Mahanta, R., Sarma, D., and Choudhury, A.: Heavy rainfall occurrences in northeast India, International Journal of Climatology, 33, 1456–1469, https://doi.org/10.1002/joc.3526, 2013.

Malardel, S.: Fondamentaux de météorologie: à l'école du temps, Cépaduès, https://books.google.de/books?id=4huTAAAACAAJ, 2005.

Malurkar, S. L.: ABNORMALLY DRY AND WET WESTERN DISTURBANCES OVER North India, Current Science, 16, 139–141, http://www.jstor.org/stable/24210723, 1947.

Mannan, M. A., Chowdhury, M. A. M., Karmakar, S., Ahmed, S., and Rahman, A.: Analysis and prediction of rainfall associated with Western Disturbances during winter months in Bangladesh, Den-Drop (A Scientific Journal of Meteorology and Geo-physics), Bangladesh Meteorological Department, Dhaka, Bangladesh, 4, 12–24, 2017.

Martínez-Alvarado, O., Joos, H., Chagnon, J., Boettcher, M., Gray, S. L., Plant, R. S., Methven, J., and Wernli, H.: The dichotomous structure of the warm conveyor belt, Quarterly Journal of the Royal Meteorological Society, 140, 1809–1824, https://doi.org/10.1002/qj.2276, 2014.

Midhuna, T. M., Kumar, P., and Dimri, A. P.: A new Western Disturbance Index for the Indian winter monsoon, Journal of Earth System Science, 129, https://doi.org/10.1007/s12040-019-1324-1, 2020.

Mujumdar, M.: Diagnostic Analysis of Wintertime Rainfall Events Over the Arabian Region, Contribution from IITM, Indian Institute of Tropical Meteorology, https://books.google.de/books?id=MHfxMQAACAAJ, 2006.

Mull, S. and Desai, B.: The Origin and Structure of the Winter Depressions of Northwest India, Technical Note 25:18, 1947.

Nathans, L., Oswald, F., and Nimon, K.: Interpreting multiple linear regression: A guidebook of variable importance, Practical Assessment, Research and Evaluation, 17, 1–19, 2012.

Pisharoty, P. and Desai, B.: Western disturbances and Indian weather, Indian J. Meteorol. Geophys, 7, 333–338, 1956.

Rakesh, V., Singh, R., Yuliya, D., Pal, P. K., and Joshi, P. C.: Impact of variational assimilation of MODIS thermodynamic profiles in the simulation of western disturbance, International Journal of Remote Sensing, 30, 4867–4887, https://doi.org/10.1080/01431160902980332, 2009.

Rana, S., McGregor, J., and Renwick, J.: Precipitation seasonality over the Indian subcontinent: An evaluation of gauge, reanalyses, and satellite retrievals, Journal of Hydrometeorology, 16, 631–651, 2015.

Sankar, N. V. and Babu, C.: Role of vorticity advection and thermal advection in the development of western disturbance during North Indian winter, Meteorology and Atmospheric Physics, 132, 515–529, 2020.

Schiemann, R., Lüthi, D., and Schär, C.: Seasonality and Interannual Variability of the Westerly Jet in the Tibetan Plateau Region., Journal of Climate, 22, 2940–2957, https://doi.org/10.1175/2008JCLI2625.1, 2009.

Singh, S. P., Bassignana-Khadka, I., Singh Karky, B., and Sharma, E.: Climate change in the Hindu Kush-Himalayas: the state of current knowledge, Tech. rep., International Centre for Integrated Mountain Development (ICIMOD), 2011.

Smith, R. L., Joel W. Ager, J., and Williams, D. L.: Suppressor Variables in Multiple Regression/Correlation, Educational and Psychological Measurement, 52, 17–29, https://doi.org/10.1177/001316449205200102, 1992.

Syed, F. S., Giorgi, F., Pal, J. S., and Keay, K.: Regional climate model simulation of winter climate over Central–Southwest Asia, with emphasis on NAO and ENSO effects, International Journal of Climatology, 30, 220–235, https://doi.org/10.1002/joc.1887, 2010.

Thapa, K., Endreny, T. A., and Ferguson, C. R.: Atmospheric Rivers Carry Nonmonsoon Extreme Precipitation Into Nepal, Journal of Geophysical Research: Atmospheres, 123, 5901–5912, https://doi.org/10.1029/2017JD027626, 2018.

705 Thomas, L., Dash, S. K., Mohanty, U. C., and Babu, C. A.: Features of western disturbances simulated over north India using different land-use data sets, Meteorological Applications, 25, 246–253, https://doi.org/10.1002/met.1687, 2018.

Tinmaker, M. and Ali, K.: Space time variation of lightning activity over northeast India, Meteorologische Zeitschrift, 21, 135–143, 2012.

Xueyuan, K. and Yaocun, Z.: Seasonal variation of the East Asian Subtropical Westerly Jet and its association with the heating field over East Asia, Advances in Atmospheric Sciences, 22, 831–840, https://doi.org/10.1007/bf02918683, 2005.

710 Yadav, R. K., Kumar, K. R., and Rajeevan, M.: Characteristic features of winter precipitation and its variability over northwest India, Journal of Earth System Science, 121, 611–623, https://doi.org/10.1007/s12040-012-0184-8, 2012.

Yang, S., Lau, K.-M., Yoo, S.-H., Kinter, J. L., Miyakoda, K., and Ho, C.-H.: Upstream Subtropical Signals Preceding the Asian Summer Monsoon Circulation, Journal of Climate, 17, 4213–4229, https://doi.org/10.1175/JCLI3192.1, 2004.

Zhu, Y. and Newell, R. E.: A Proposed Algorithm for Moisture Fluxes from Atmospheric Rivers, Monthly Weather Review, 126, 725–735,
715 https://doi.org/10.1175/1520-0493(1998)126<0725:APAFMF>2.0.CO;2, 1998.